

Stationary versus Bifurcation regime for Standing Wave Central Pattern Generator[☆]

R. Martin-del-Campo^{a,*}, E. Jonckheere^a

^a*Electrical Engineering Dept., University of Southern California, Los Angeles, CA 90089-2563, United States*

Abstract

The purpose of this research is to show that the correlation analysis on surface Electromyographic (sEMG) signals that originally confirmed existence of a standing wave Central Pattern Generator (CPG) along the spine are reproducible despite evolution of the entrainment technique, different hardware and data collection protocol. Moreover, as major novelty of the research, it is shown that this CPG can undergo bifurcation. The visually intuitive manifestation of the bifurcation is statistically confirmed—using bootstrap analysis—by showing that the standing wave occurs on different subbands of the Daubechies DB3 wavelet decomposition of the sEMG signals.

Keywords: Central Pattern Generator; Surface Electromyography; Bifurcation; Coherence; Wavelets; Bootstrapping

1. Introduction

The so-called *spinal wave* is a visually obvious phenomenon during which the spine goes through a rhythmic [1] oscillation elicited by light finger pressure at some sensitized areas of the spine, typically, the neck and the sacrum. As argued

[☆]Research approved by the Institutional Review Board (IRB) of the University of Southern California and supported by the Global Gateway Foundation.

*Corresponding author at: 3819 Flower Dr., Apt 7, Los Angeles, CA 90037-1320, United States. Tel.: +1 213 290 2315.

Email addresses: mart737@usc.edu (R. Martin-del-Campo), jonckhee@usc.edu (E. Jonckheere)

URL: <http://eudoxus2.usc.edu> (E. Jonckheere)

in our original work [2], Alf Breig's dural-vertebral attachments [3] close sensory-motor loops in both the neck and the sacrum, creating localized oscillations, which soon propagate along the spine to settle in a standing wave pattern. The crucial features that the movement is rhythmic, that it becomes self-sustained after some entrainment, hence has no sensory input, already point to a Central Pattern Generator (CPG), a concept that is still an active area of research [4]. Moreover, as reported in the earlier paper [2], a quadriplegic subject with a C2-C3 injury was able to experience some spinal wave pattern, which indicates that the CPG circuitry is embedded in the spine. It therefore appears that this movement is, next to gait, another human CPG.

A standing wave oscillation is certainly a manifestation of *coherence* in the neuro-skeletal system. Since the spinal standing wave has its coherence extending from the neck to the sacrum, it is fair to say that this is a phenomenon of *coherence at a distance*. Coherence at a distance between EEG and/or (s)EMG signals is considered to be an attribute of a properly functioning nervous system. The evidence that we presented in support of this paradigm is the deterioration of coherence in a quadriplegic subject compared with a control subject [2].

The purpose of this paper is two-fold. First (Case Study I), we show that the early results [2] upon which the CPG hypothesis rests are reproducible. Second (Case Study II), we show that the spinal wave CPG, in addition to the classical attributes associated with a CPG, can undergo bifurcation.

Nearly 10 years separate the data collection upon which [2] is based from the present one. During that time, the entrainment technique evolved to make the movement better controllable (the sEMG signals can be made smooth or bursty at will), the electrode positioning underwent some slight changes while we experienced with different orientation of the differential amplifier input prongs relative to muscle fibers, and the hardware (front-end electronics together with sEMG amplifiers) was upgraded. The software underwent some upgrade as well. Despite these changes and a 10-year span between the two experiments, we show in Case Study I that the results are consistent.

As argued in [2], what constitutes a CPG is still debatable. Here, in Case

Study II, we add one more attribute that can be associated with a CPG: the ability to undergo bifurcations [5]. When the subject experiences this bifurcation, some structural changes (e.g., mode shape) in the rhythmic oscillations of the spine are evident to the naked eye. This occurs with a concomitant visually obvious discontinuity in the sEMG signals. Objectively, the bifurcation is confirmed by observing that the correlation pattern among the cervical, thoracic, lumbar and sacral sEMG signals consistent with a standing wave occurs at different subbands of the Daubechies DB3 wavelet decomposition of the sEMG signals.

In the case the signals are analysed across a bifurcation, the correlation pattern that reveals coherence cannot be expected to be as crisp as either that of [2] or that of Case-Study I of the present paper, both of which can be considered ideal, “textbook” examples. As such, another purpose of Case-Study II of the present paper is to assess by how much the correlation pattern deviates from those of [2] when conditions are no longer ideal.

2. Methods

The control subjects of the two cases studies presented here are both healthy individuals who, prior to recordings, had signed the informed consent form approved by the Institutional Review Board (IRB) of the University of Southern California. Surface Electromyography (sEMG) reduced-noise tripolar electrodes were placed at cervical (C2-C3), thoracic (T4-T6), lumbar (L3), and sacral (S2-S4) positions. The sensitive input prongs of the front-end electronics were aligned with the back muscle fibers [6]. The sEMG signals were amplified by an Insight Subluxation Station, Discovery model. The analog-to-digital conversion was done by a USB-1608FS card manufactured by Measurement ComputingTM and running on a Windows XP platform.

During Case Study I, 720,000 samples were recorded at a rate of 4 kHz as shown in Figure 1. The analysis was centred around a section of 100 000 samples, where a phenomenon of synchronicity of signals is visually evident from Figure

2, between 70,000 and 80,000 samples.

The procedure related to Case Study II was similar. Three seconds of data were analyzed using the same sampling rate as Case Study I. This section comprises a set of 12,000 samples, in which the bifurcation is present.

To highlight the differences between the protocol of the earlier study [2] and the protocol utilized to collect the data of Case-Studies I & II, we observe, first, that the sensitive prongs of the electrode front-end electronics were put at a 45 deg. angle relative to spine in the earlier study, as opposed to aligned with the fibers here. Second, the sacral electrode was positioned on the gluteus, as opposed to the sacrum as reported here. Third, the sEMG signals were amplified by an older Insight Millennium sEMG machine and the analog-to-digital conversion was done with a PC-Card DAS16/16, manufactured by Computer Boards (now Measurement ComputingTM), running on a Windows 98 operating system, as opposed to the upgraded equipment utilized here.

Let $y_1(k)$, $y_2(k)$, $y_3(k)$, $y_4(k)$ be either the D₈ or the D₇ subband of the cervical, thoracic, lumbar and sacral signals, resp., sEMG signals. As in [2], we define the correlations

$$r_{ij}(s) = \frac{\sum_{k=1}^{K-s} (y_i(k) - \bar{y}_i)(y_j(k+s) - \bar{y}_j)}{\sqrt{\sum_{k=1}^{K-s} (y_i(k) - \bar{y}_i)^2} \sqrt{\sum_{k=1}^{K-s} (y_j(k) - \bar{y}_j)^2}}$$

As argued in [2], the movement has a coherent standing wave if there exist some delays $s_1 < s_2 < \dots$ such that

$$r_{ij}(s_\ell) = 0; \quad i, j = 1, 2, 3, 4; \quad \ell = 1, 2, \dots$$

The points s_ℓ , $\ell = 1, 2, \dots$, have been called *zero correlation nodes* and are manifestations of a coherent standing wave. Clearly, one cannot expect a perfectly coherent standing wave and the above will not, in general, hold for all ℓ 's. In practice, one can expect the above to hold reasonably accurately for $\ell = 1$; the accuracy already deteriorates for $\ell = 2$, and in general we no longer look at the above for $\ell > 2$.

3. Results: Case Study I

The raw sEMG signals from the 4 electrodes are shown in Figure 1.

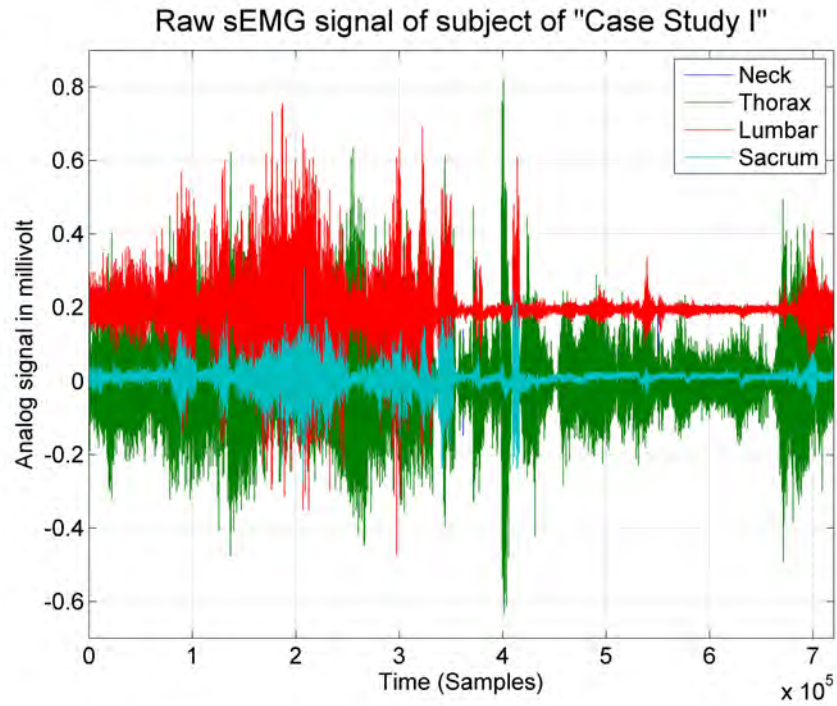


Figure 1: Raw sEMG data at Neck, Thorax, Lumbar and Sacrum of Case Study I

Eyeball inspection of the sEMG traces of Figure 1 already shows some coherence as there is evidence that the signals are bursting synchronously. For example, it suffices to look at the simultaneous bursting of 3 signals around 700,000 samples to see some coherence. However, for the sake of the coherence analysis, we focus our attention on the segment between samples 270,000 and 370,000. This section of raw sEMG is plotted in Figure 2

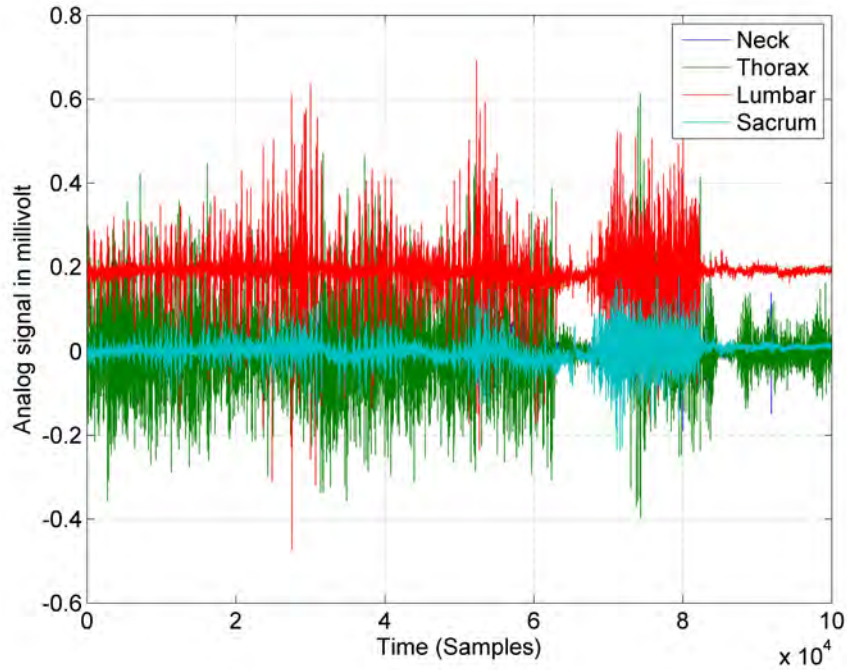


Figure 2: Section from sample 270,000 to 370,000 of raw sEMG data of Case Study I at Neck, Thorax, Lumbar and Sacrum

Again, some synchronous bursting is visually obvious from Figure 2. Note that this bursty signal does not look quite like the one of Figure 1 of [2], which is much smoother. Nevertheless, the coherence results *remain the same*.

A summary of the D_8 subbands of the Daubechies DB3 wavelet decomposition of the 4 signals is shown in Figure 3. Most importantly, observe—quite consistently with Figure 2 of [2]—the synchronization doublet around sample 65,000 of the sacral signal (marked with a circle).

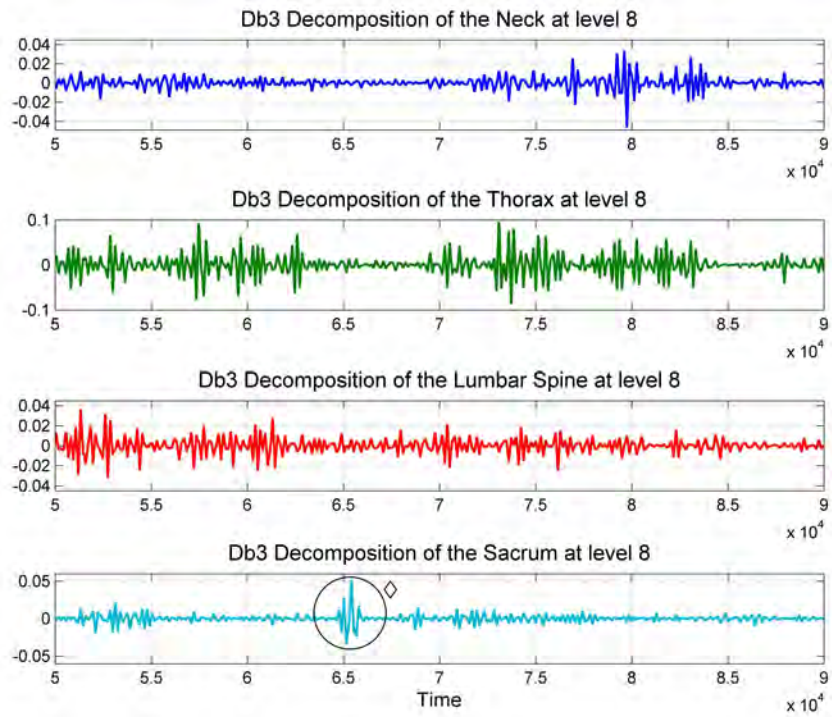
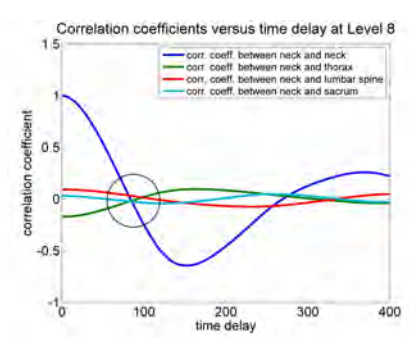
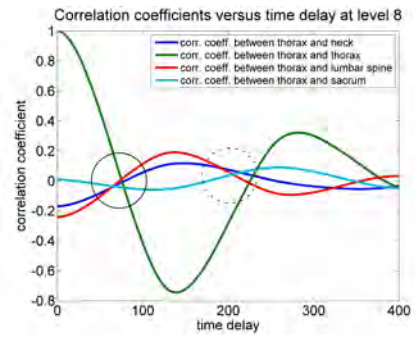


Figure 3: D_8 subbands of Daubechies DB3 wavelet decomposition of Neck, Thorax, Lumbar and Sacrum, respectively

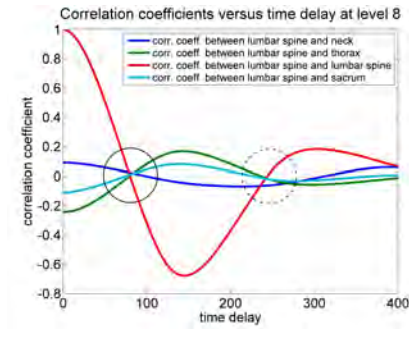
The cross-correlation between the four different sEMG signals obtained from subband D_8 is shown in Figure 4.



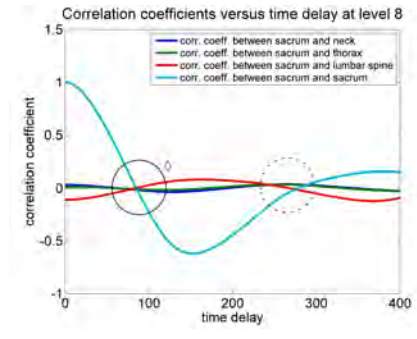
(a) Correlation between D_8 subbands of neck and other signals of control. Blue line: neck-neck correlation; green line: neck-thorax correlation; red line: neck-lumbar correlation; cyan line: neck-sacrum correlation.



(b) Correlation between D_8 subbands of thorax and other signals of control. Blue line: thorax-neck correlation; green line: thorax-thorax correlation; red line: thorax-lumbar correlation; cyan line: thorax-sacrum correlation.



(c) Correlation between D_8 subbands of lumbar and other signals of control. Blue line: lumbar-neck correlation; green line: lumbar-thorax correlation; red line: lumbar-lumbar correlation; cyan line: lumbar-sacrum correlation.



(d) Correlation between D_8 subbands of sacrum and other signals of control. Blue line: sacrum-neck correlation; green line: sacrum-thorax correlation; red line: sacrum-lumbar correlation; cyan line: sacrum-sacrum correlation.

Figure 4: Correlation on D_8 subband among the 4 signals from sample 270,000 to 370,000 of Case Study I.

The plots from Figures 4a-4d are quite similar to those of the left panels of

Figures 3-6 of [2]. The s_1 zero correlation nodes (marked with black circles) develop with the same level of accuracy as in [2], while the s_2 nodes (marked with dotted circles) can be seen, but not as markedly as the s_1 node, exactly as in [2].

4. Results: Zero correlation nodes: Case Study II

The raw sEMG data recorded for this case study is shown in Figure 5 for neck and thorax signals.

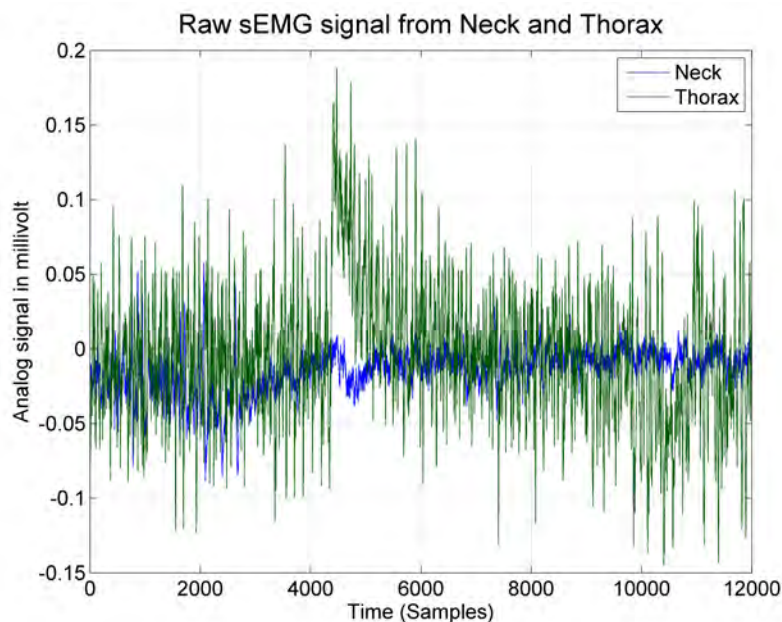


Figure 5: Raw sEMG data obtained from Neck and Thorax, of Case Study II.

Between samples 4,300 and 5,300, the signals exhibit a clear discontinuity, with an obvious lack of correlation between the neck and the thorax signals. Remarkably, this discontinuity in the sEMG traces occurred *exactly* at the time the practitioner, who had no visual contact with the real-time oscilloscopic display of the sEMG signals, called a visually observable change in the structural properties of the spinal wave.

The analysis is broken down in two parts: First, before the bifurcation, i.e., from sample 1 until sample 4,000. Second, after the bifurcation, that is, between sample 5,411 and sample 9,871. Thus, the specific section comprised within the bifurcation is deliberately avoided, namely, between samples 4,300 and 5,300.

The specificity of the sEMG signals is best observed in the wavelet packets in the D_6 , D_7 and D_8 subbands of the DB3 decomposition, as it is shown in Figures 6, 7, 8 and 9. The cases of synchronization doublets consistent with zero correlation nodes are identified with circles.

4.1. Analysis before the bifurcation

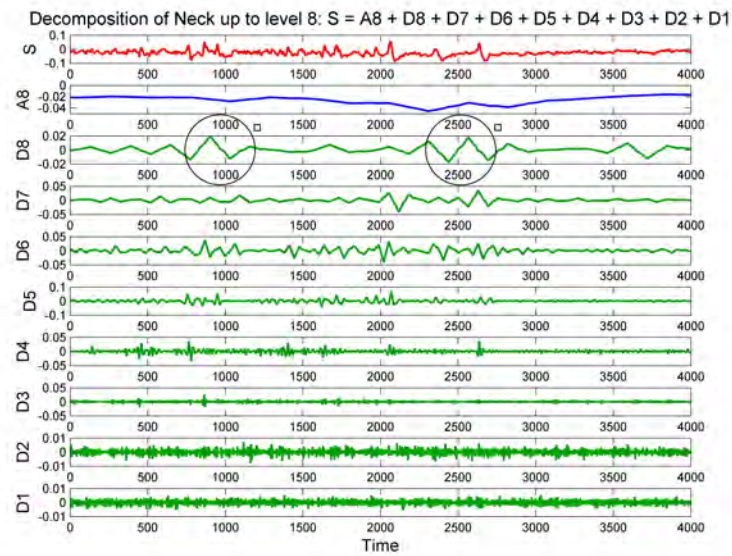


Figure 6: DB3 decomposition of Neck signal before the bifurcation of Case Study II.

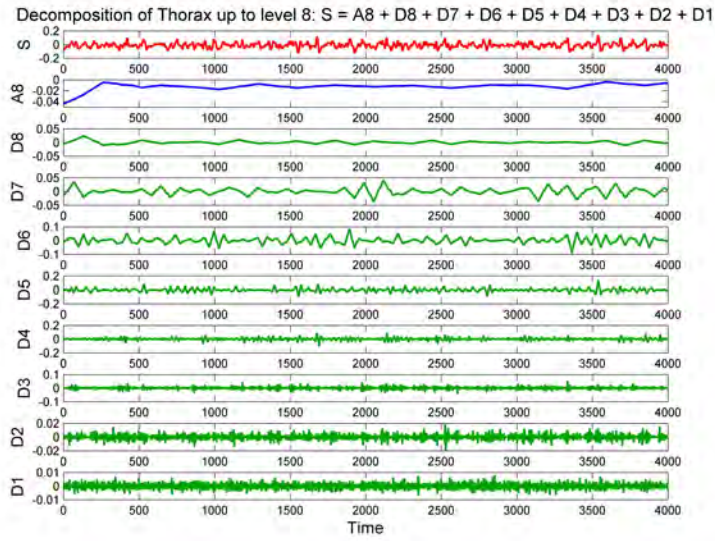


Figure 7: DB3 decomposition of Thorax signal before the bifurcation of Case Study II.

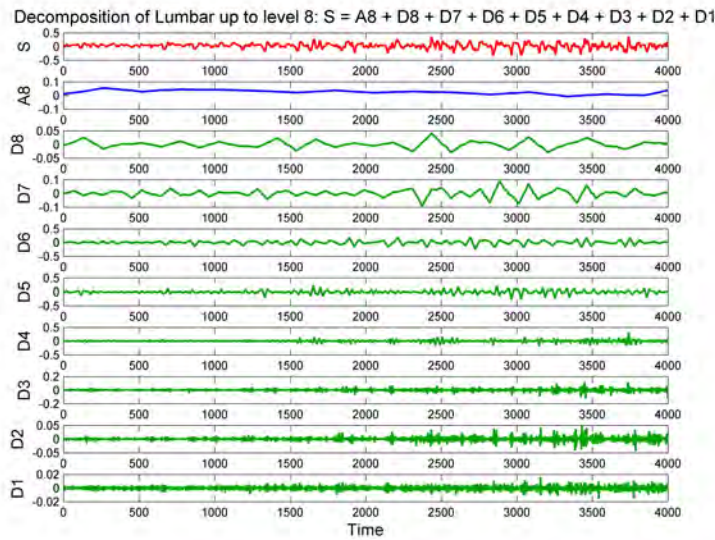


Figure 8: DB3 decomposition of Lumbar signal before the bifurcation of Case Study II.

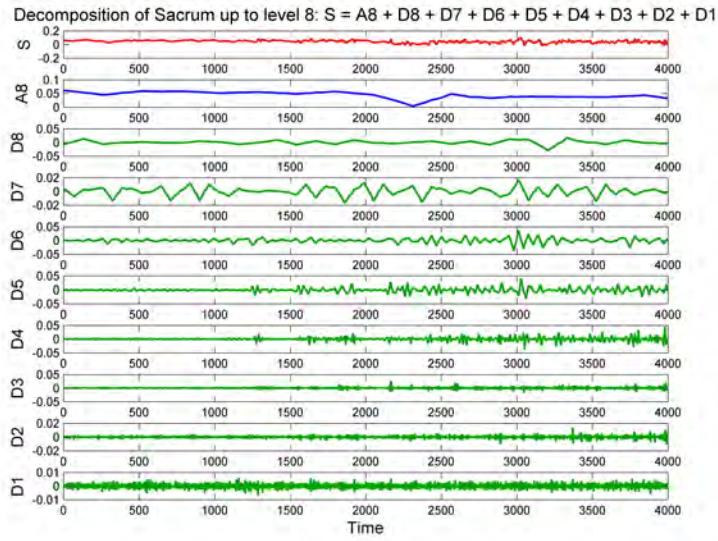


Figure 9: DB3 decomposition of Sacral signal before the bifurcation of Case Study II.

A top (neck) to bottom (sacrum) summary redisplay of this wavelet decomposition before the bifurcation on the relevant D_8 , D_7 and D_6 subband signals is shown in Figures 10, 11 and 12 respectively. Again, the synchronization doublets consistent with zero correlation nodes are identified with circles.

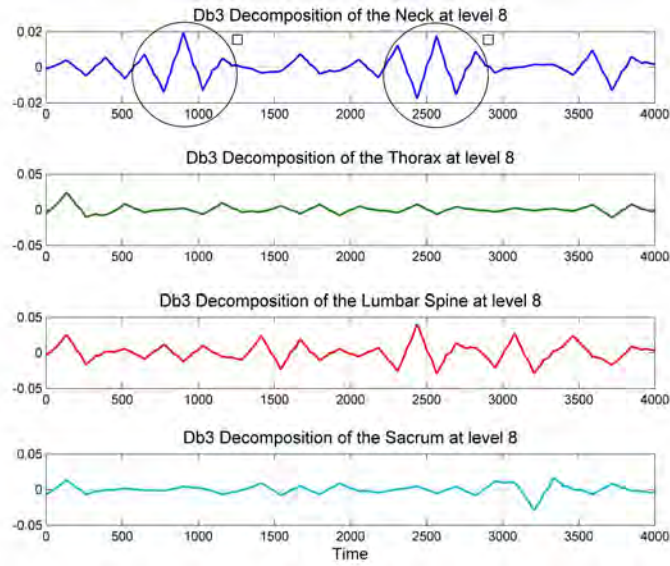


Figure 10: DB3 decomposition of top to bottom signals on D_8 subband before the bifurcation of Case Study II.

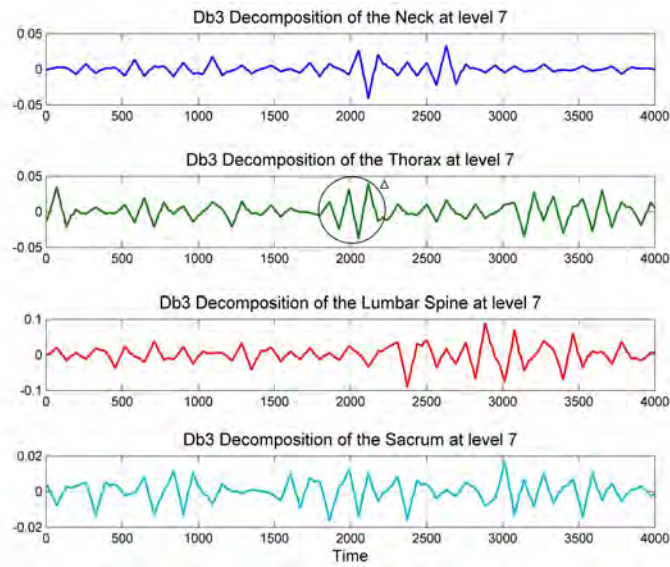


Figure 11: DB3 decomposition of top to bottom signals on D_7 subband before the bifurcation of Case Study II.

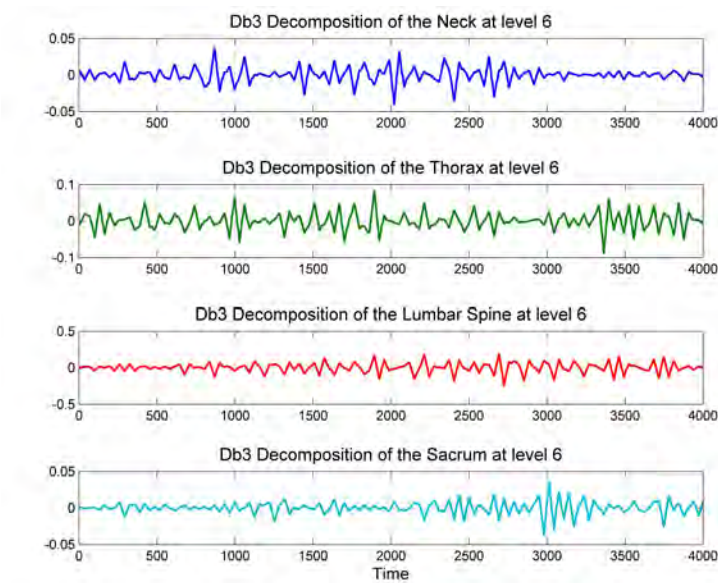
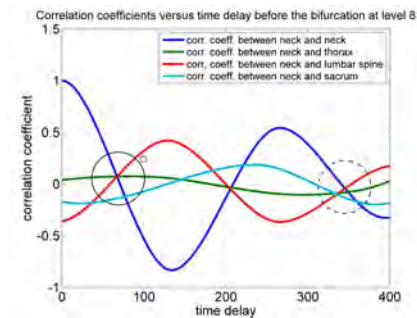
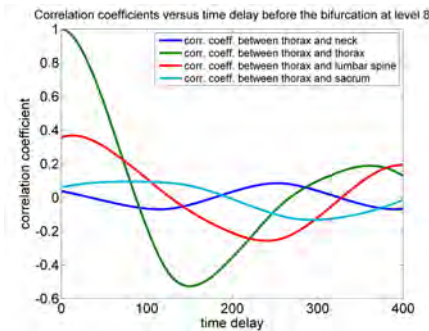


Figure 12: DB3 decomposition of top to bottom signals on D_6 subband before the bifurcation of Case Study II.

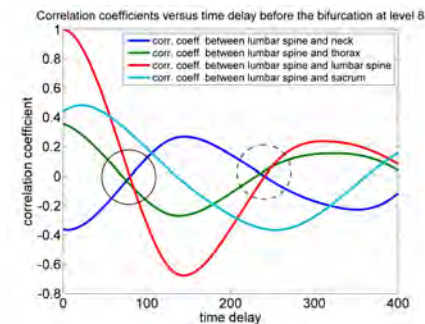
The correlation plots before the bifurcation of the D_8 , D_7 , D_6 subbands are shown in Figures 13, 14 and 15, respectively. On the D_8 , for some reason, the thoracic correlation plots do not show coherence. The sacral curve shows some aberration because of the sacral electrode positioning (not the same as that of [2].) On the D_7 , not much correlation can be seen, except for the thoracic plots. On the D_6 , not much correlation can be seen. (On the lumbar plots, there *appears* to be a crossing, but it is too far off the $r = 0$ axis to be of any significance.)



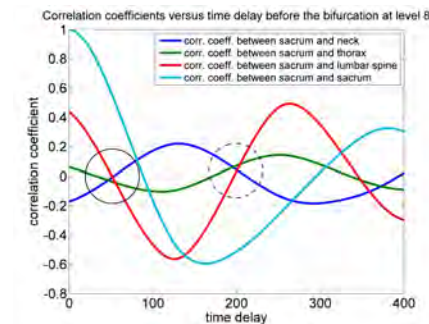
(a) Correlation between D_8 subbands of neck and other signals of control. Blue line: neck-neck correlation; green line: neck-thorax correlation; red line: neck-lumbar correlation; cyan line: neck-sacrum correlation.



(b) Correlation between D_8 subbands of thorax and other signals of control. Blue line: thorax-neck correlation; green line: thorax-thorax correlation; red line: thorax-lumbar correlation; cyan line: thorax-sacrum correlation.

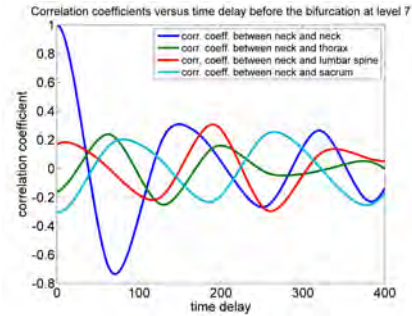


(c) Correlation between D_8 subbands of lumbar and other signals of control. Blue line: lumbar-neck correlation; green line: lumbar-thorax correlation; red line: lumbar-lumbar correlation; cyan line: lumbar-sacrum correlation.

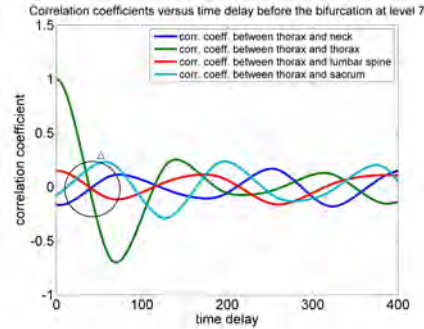


(d) Correlation between D_8 subbands of sacrum and other signals of control. Blue line: sacrum-neck correlation; green line: sacrum-thorax correlation; red line: sacrum-lumbar correlation; cyan line: sacrum-sacrum correlation.

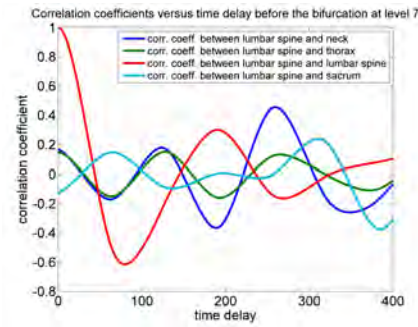
Figure 13: Correlation on D_8 subband of top to bottom signals before the bifurcation of Case Study II.



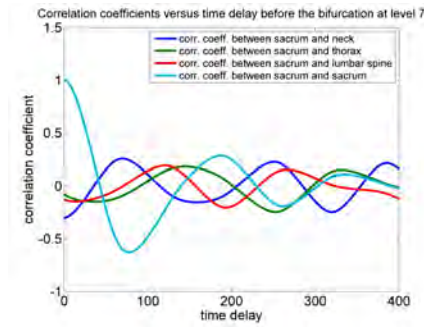
(a) Correlation between D_7 subbands of neck and other signals of control. Blue line: neck-neck correlation; green line: neck-thorax correlation; red line: neck-lumbar correlation; cyan line: neck-sacrum correlation.



(b) Correlation between D_7 subbands of thorax and other signals of control. Blue line: thorax-neck correlation; green line: thorax-thorax correlation; red line: thorax-lumbar correlation; cyan line: thorax-sacrum correlation.

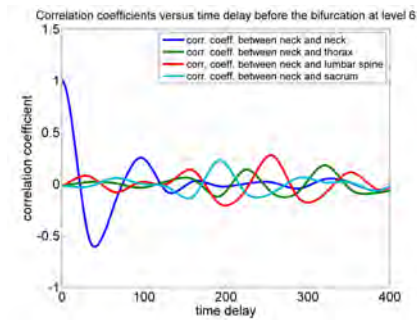


(c) Correlation between D_7 subbands of lumbar and other signals of control. Blue line: lumbar-neck correlation; green line: lumbar-thorax correlation; red line: lumbar-lumbar correlation; cyan line: lumbar-sacrum correlation.

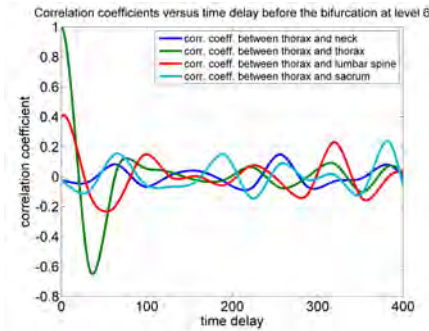


(d) Correlation between D_7 subbands of sacrum and other signals of control. Blue line: sacrum-neck correlation; green line: sacrum-thorax correlation; red line: sacrum-lumbar correlation; cyan line: sacrum-sacrum correlation.

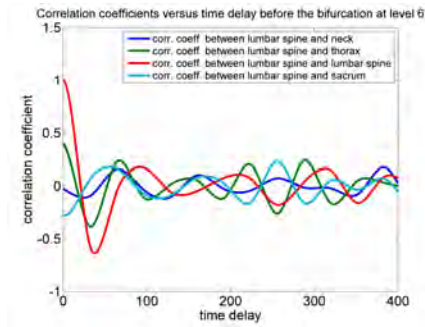
Figure 14: Correlation on D_7 subband of top to bottom signals before the bifurcation of Case Study II.



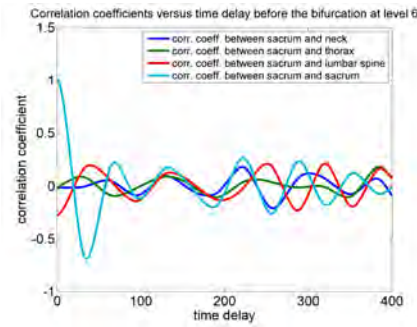
(a) Correlation between D_6 subbands of neck and other signals of control. Blue line: neck-neck correlation; green line: neck-thorax correlation; red line: neck-lumbar correlation; cyan line: neck-sacrum correlation.



(b) Correlation between D_6 subbands of thorax and other signals of control. Blue line: thorax-neck correlation; green line: thorax-thorax correlation; red line: thorax-lumbar correlation; cyan line: thorax-sacrum correlation.



(c) Correlation between D_6 subbands of lumbar and other signals of control. Blue line: lumbar-neck correlation; green line: lumbar-thorax correlation; red line: lumbar-lumbar correlation; cyan line: lumbar-sacrum correlation.



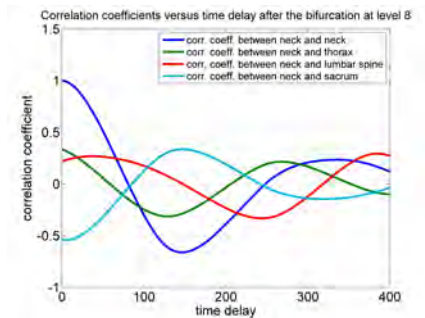
(d) Correlation between D_6 subbands of sacrum and other signals of control. Blue line: sacrum-neck correlation; green line: sacrum-thorax correlation; red line: sacrum-lumbar correlation; cyan line: sacrum-sacrum correlation.

Figure 15: Correlation on D_6 subband of top to bottom signals before the bifurcation of Case Study II.

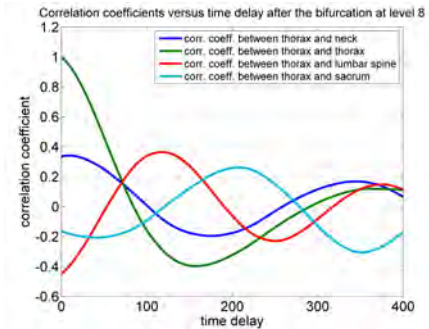
4.2. Analysis after the bifurcation

The same procedure was performed right after the section where the bifurcation phenomenon terminates, and comprises approximately one second of the sEMG trace, (from 5,411 to 9,871 samples). As in the previous case (before the bifurcation), the wavelet packets were also best observed on the D_8 , D_7 and D_6 subbands. The corresponding correlation plots after the bifurcation are shown in Figures 16, 17 and 18.

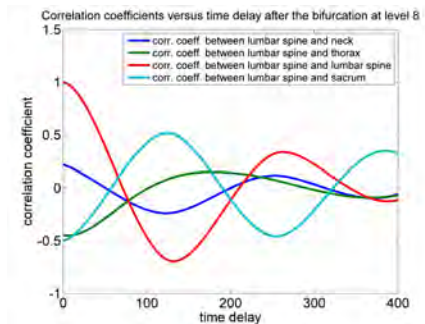
On the D_8 subband, not much correlation can be seen, except possible on the sacral curves (see black circle). The D_7 subband shows several s_1 nodes and even higher zero crossing nodes. The D_6 does not appear to show any zero correlation nodes.



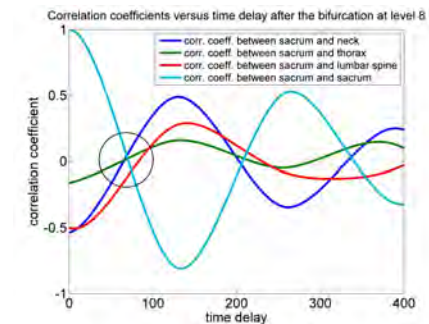
(a) Correlation between D_8 subbands of neck and other signals of control. Blue line: neck-neck correlation; green line: neck-thorax correlation; red line: neck-lumbar correlation; cyan line: neck-sacrum correlation.



(b) Correlation between D_8 subbands of thorax and other signals of control. Blue line: thorax-neck correlation; green line: thorax-thorax correlation; red line: thorax-lumbar correlation; cyan line: thorax-sacrum correlation.

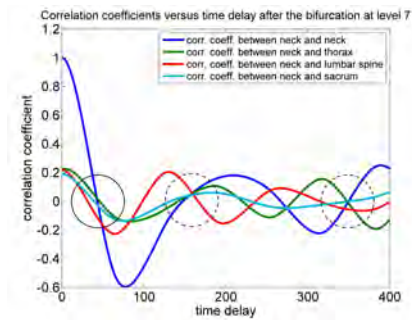


(c) Correlation between D_8 subbands of lumbar and other signals of control. Blue line: lumbar-neck correlation; green line: lumbar-thorax correlation; red line: lumbar-lumbar correlation; cyan line: lumbar-sacrum correlation.

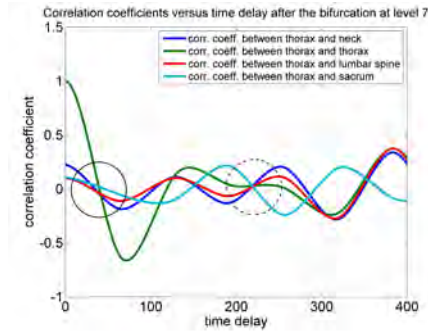


(d) Correlation between D_8 subbands of sacrum and other signals of control. Blue line: sacrum-neck correlation; green line: sacrum-thorax correlation; red line: sacrum-lumbar correlation; cyan line: sacrum-sacrum correlation.

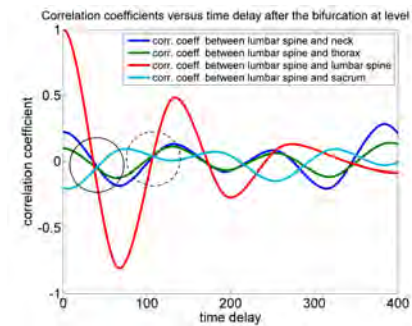
Figure 16: Correlation plots on D_8 subband of top to bottom signals after the bifurcation of Case Study II.



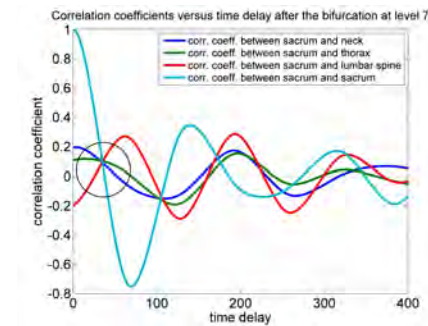
(a) Correlation between D_7 subbands of neck and other signals of control. Blue line: neck-neck correlation; green line: neck-thorax correlation; red line: neck-lumbar correlation; cyan line: neck-sacrum correlation.



(b) Correlation between D_7 subbands of thorax and other signals of control. Blue line: thorax-neck correlation; green line: thorax-thorax correlation; red line: thorax-lumbar correlation; cyan line: thorax-sacrum correlation.

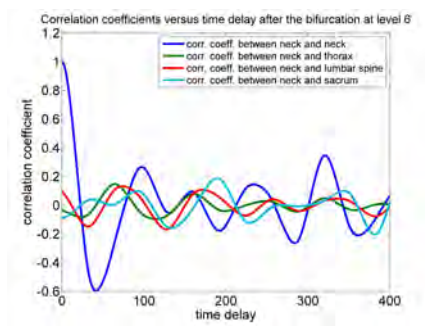


(c) Correlation between D_7 subbands of lumbar and other signals of control. Blue line: lumbar-neck correlation; green line: lumbar-thorax correlation; red line: lumbar-lumbar correlation; cyan line: lumbar-sacrum correlation.

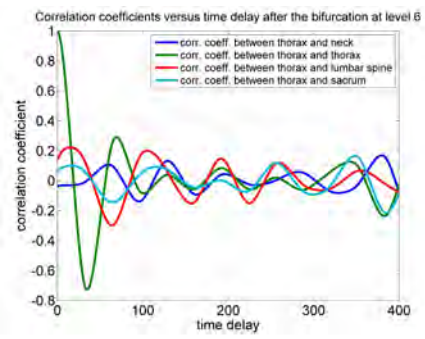


(d) Correlation between D_7 subbands of sacrum and other signals of control. Blue line: sacrum-neck correlation; green line: sacrum-thorax correlation; red line: sacrum-lumbar correlation; cyan line: sacrum-sacrum correlation.

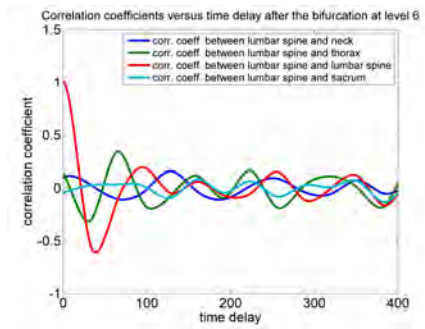
Figure 17: Correlation plots on D_7 subband of top to bottom signals after the bifurcation of Case Study II.



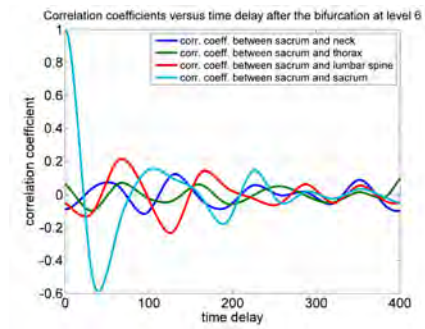
(a) Correlation between D_6 subbands of neck and other signals of control. Blue line: neck-neck correlation; green line: neck-thorax correlation; red line: neck-lumbar correlation; cyan line: neck-sacrum correlation.



(b) Correlation between D_6 subbands of thorax and other signals of control. Blue line: thorax-neck correlation; green line: thorax-thorax correlation; red line: thorax-lumbar correlation; cyan line: thorax-sacrum correlation.



(c) Correlation between D_6 subbands of lumbar and other signals of control. Blue line: lumbar-neck correlation; green line: lumbar-thorax correlation; red line: lumbar-lumbar correlation; cyan line: lumbar-sacrum correlation.



(d) Correlation between D_6 subbands of sacrum and other signals of control. Blue line: sacrum-neck correlation; green line: sacrum-thorax correlation; red line: sacrum-lumbar correlation; cyan line: sacrum-sacrum correlation.

Figure 18: Correlation plots on D_6 subband of top to bottom signals after the bifurcation of Case Study II.

5. Results: Shift in cross spectral density: Case Study II

It can be observed in Figures 13, 14, 16 and 17 that the “slow” D₈ sub-band shows a larger correlation than the D₇ sub-band *before the bifurcation*, and the “faster” D₇ sub-band shows a larger correlation than the D₈ sub-band *after the bifurcation*. Thus, we expect the *cross Power Spectral Density (cPSD)* between the signals along the spine to be larger in high frequency *after the bifurcation*. Equivalently, we expect the *cPSD* to be larger in low frequency *before the bifurcation*. This “educated guess” best fits the data only for the lower spinal signals and is confirmed by a statistical test of significance that we endeavored to develop specially for this case.

After obtaining the cPSD of the spine signals, that is, the frequency distribution of the correlation between the 16 possible combinations of two out of four spine signals, we come up with a *qualitative* behavior of the cPSD across the bifurcation for the lower spinal signals as shown in Figure 19.

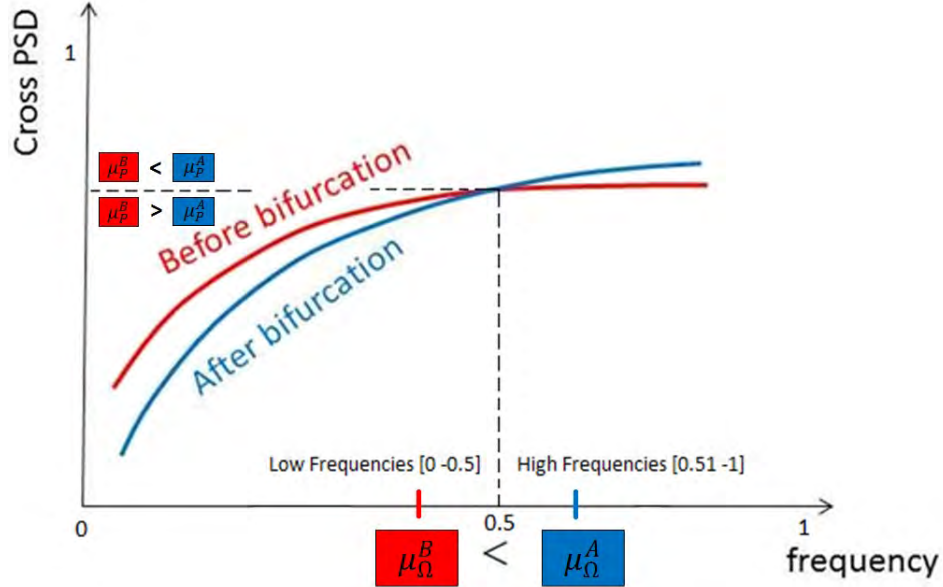


Figure 19: Qualitative behavior of the cross Power Spectral Densities (cPSD) against the frequency for the lower spine signals Before (red) and After (blue) the bifurcation.

The randomness is analyzed in terms of the normalized cPSDs values, and we define the “Before” and “After” probability density functions, $f_P^B(\rho)$, $f_P^A(\rho)$, respectively. Let μ_P^B , μ_P^A be the means of $f_P^B(\rho)$, $f_P^A(\rho)$, respectively. To statistically analyze the existence of the crossing between the red and blue curves from Figure 19, the test was broken down into low normalized frequencies, from 0 to 0.5, and high normalized frequencies, from 0.51 to 1. It suffices to show that, statistically, there is enough confidence in asserting that $\mu_P^B < \mu_P^A$ at high frequencies and $\mu_P^B > \mu_P^A$ at low frequencies.

5.1. Prelude: test of significance under Gauss assumption

Since we focus our attention on the randomness along the range of cPSD values, we statistically define $\rho_1^B, \rho_2^B, \rho_3^B, \dots, \rho_m^B$ as a random draw from $f_P^B(\rho)$ along the Y -axis. Define the “Before” and “After” means as

$$\bar{\rho}^B = \frac{1}{m} \sum_{i=1}^m \rho_i^B, \quad \bar{\rho}^A = \frac{1}{m} \sum_{i=1}^m \rho_i^A.$$

Define the “total sampled variances:”

$$(S^B)^2 = \frac{1}{m-1} \sum_{i=1}^m (\rho_i^B - \bar{\rho}^B)^2, \quad (S^A)^2 = \frac{1}{m-1} \sum_{i=1}^m (\rho_i^A - \bar{\rho}^A)^2.$$

It turns out that, under Gauss assumption on the normalized cPSDs, $f_P^B(\rho)$ and $f_P^A(\rho)$, the quantity

$$t = \frac{\bar{\rho}^B - \bar{\rho}^A}{\sqrt{\frac{(S^B)^2 + (S^A)^2}{m}}}$$

has approximately a t -distribution[7], and becomes Gaussian for m large. We want to show that $\mu_P^B < \mu_P^A$ at high frequencies and $\mu_P^B > \mu_P^A$ at low frequencies, statistically speaking, $\bar{\rho}^B - \bar{\rho}^A < 0$ and $\bar{\rho}^B - \bar{\rho}^A > 0$ respectively.

The problem is that our investigations have shown that $f_P^B(\rho)$, $f_P^A(\rho)$ do not follow the Gauss distribution. Thus, to go around the lack of Gaussian property of $f_P^B(\rho)$, $f_P^A(\rho)$, we need to perform bootstrapping of cPSDs values.

5.2. No Gauss assumption: bootstrapping

Bootstrapping is a Monte Carlo method[8] that employs repeated samples with replacement from the original data. This testing procedure is useful when

the theoretical distribution of the statistic is complicated—as in our case—or unknown. Using bootstrapping, we conducted a statistical test of hypothesis to estimate the Achieved Significance Level (ASL) of the test, also known as *p-value*.

We begin by calculating the value of the test statistic for the sample,

$$t_{calc} = \frac{\bar{\rho}^B - \bar{\rho}^A}{\sqrt{\frac{(S^B)^2 + (S^A)^2}{m}}}.$$

Then we randomly sample a total of j times, with replacement, and transform m values from the sample as $x_i^B = \rho_i^B - \bar{\rho}^B + \bar{\rho}$ and the sample $x_i^A = \rho_i^A - \bar{\rho}^A + \bar{\rho}$, where $\bar{\rho}$ is the mean of the combined samples.

For each bootstrap sample j , we compute the test statistic

$$t_j = \frac{\bar{x}^B - \bar{x}^A}{\sqrt{\frac{(S^B)^2 + (S^A)^2}{m}}},$$

where \bar{x}^B and \bar{x}^A are the means of bootstrap sample j for sample x_i^B and x_i^A , respectively.

Next, we find the bootstrap estimated *p-value*, with *Null Hypothesis* H_0 , as follows:

$$H_0 : (\mu_P^B - \mu_P^A) = 0.$$

and we define the *Alternative Hypotheses*:

$$\text{Upper-tailed test } (H_a : (\mu_P^B - \mu_P^A) > 0) : \quad ASL = \frac{\text{Number of times } t_j > t_{calc}}{j}$$

$$\text{Lower-tailed test } (H_a : (\mu_P^B - \mu_P^A) < 0) : \quad ASL = \frac{\text{Number of times } t_j < t_{calc}}{j}$$

The Bootstrapping procedure described above was implemented on MatLab, and it was run ten different times for each $j = 100$, $j = 1,000$, $j = 10,000$, $j = 100,000$, and $j = 1,000,000$ bootstrap samples from the cPSD of every combination of signals at low and high frequencies. In the Appendix section, Figures Appendix A.1-Appendix A.32 show the average of the *p-values* for every j . The *p-values* converge to a stable value as the number of bootstrap samples increases and the Standard Deviation decreases. In addition, this bootstrap

analysis was also run on JMP Pro 11, a statistical software developed by the SAS Institute; using $j = 10,000$, we obtained similar p -values as those of the MatLab bootstrap analysis. Both p -values are reported in Tables 1 and 2.

We decided to reject the Null Hypothesis when the p -value fell below 0.05. In Tables 1 and 2, we highlight those tests that significantly concur, with 95% confidence level, with the qualitative behavior gleaned from Figure 19.

Upper Spine Signals					
Neck	Neck & Neck BEFORE VS AFTER				
	Frequencies	Alternative Hypothesis	P-values calculated using:		Conclusion
			MatLab	JMP	
	Low	$H_a: \mu_{Before} < \mu_{After}$	0.02815 (S.D. = 0.000212)	0.03	Accept H_a
	High	$H_a: \mu_{Before} > \mu_{After}$	0.00075 (S.D. = 0.0000527)	0.0014	Accept H_a
	Neck & Thorax BEFORE VS AFTER				
	Frequencies	Alternative Hypothesis	P-values calculated using:		Conclusion
			MatLab	JMP	
	Low	$H_a: \mu_{Before} < \mu_{After}$	0.0851 (S.D. = 0.000270801)	0.0861	Accept H_0
	High	$H_a: \mu_{Before} > \mu_{After}$	0.56888 (S.D. = 0.000332666)	0.5678	Accept H_0
	Neck & Lumbar BEFORE VS AFTER				
	Frequencies	Alternative Hypothesis	P-values calculated using:		Conclusion
			MatLab	JMP	
	Low	$H_a: \mu_{Before} < \mu_{After}$	0.04734 (S.D. = 0.000117379)	0.0456	Accept H_a
	High	$H_a: \mu_{Before} > \mu_{After}$	0.0000 (S.D. = 0.0000)	0.0001	Accept H_a
	Neck & Sacrum BEFORE VS AFTER				
Frequencies	Alternative Hypothesis	P-values calculated using:		Conclusion	
		MatLab	JMP		
Low	$H_a: \mu_{Before} > \mu_{After}$	0.00332 (S.D. = 0.00004216)	0.0030	Accept H_a	
High	$H_a: \mu_{Before} < \mu_{After}$	0.00199 (S.D. = 0.00005676)	0.002	Accept H_a	
Thorax	Thorax & Neck BEFORE VS AFTER				
	Frequencies	Alternative Hypothesis	P-values calculated using:		Conclusion
			MatLab	JMP	
	Low	$H_a: \mu_{Before} < \mu_{After}$	0.08504 (S.D. = 0.0002319)	0.0861	Accept H_0
	High	$H_a: \mu_{Before} < \mu_{After}$	0.4311 (S.D. = 0.000505525)	0.4322	Accept H_0
	Thorax & Thorax BEFORE VS AFTER				
	Frequencies	Alternative Hypothesis	P-values calculated using:		Conclusion
			MatLab	JMP	
	Low	$H_a: \mu_{Before} < \mu_{After}$	0.07255 (S.D. = 0.000236878)	0.0725	Accept H_0
	High	$H_a: \mu_{Before} < \mu_{After}$	0.05179 (S.D. = 0.000172884)	0.0517	Accept H_0
	Thorax & Lumbar BEFORE VS AFTER				
	Frequencies	Alternative Hypothesis	P-values calculated using:		Conclusion
			MatLab	JMP	
	Low	$H_a: \mu_{Before} > \mu_{After}$	0.42737 (S.D. = 0.000386005)	0.4271	Accept H_0
	High	$H_a: \mu_{Before} < \mu_{After}$	0.0000 (S.D. = 0.0000)	0.0001	Accept H_a
	Thorax & Sacrum BEFORE VS AFTER				
Frequencies	Alternative Hypothesis	P-values calculated using:		Conclusion	
		MatLab	JMP		
Low	$H_a: \mu_{Before} > \mu_{After}$	0.0000 (S.D. = 0.0000)	0.0001	Accept H_a	
High	$H_a: \mu_{Before} > \mu_{After}$	0.0000 (S.D. = 0.0000)	0.0001	Accept H_a	

Table 1: P-values of the bootstrap statistical test from the upper spine signals.

Lower Spine Signals					
Lumbar	Lumbar & Neck BEFORE VS AFTER				
	Frequencies	Alternative Hypothesis	P-values calculated using:		Conclusion
			MatLab	JMP	
	Low	$H_a: \mu_{Before} > \mu_{After}$	0.04732 (S.D. = 0.000297396)	0.0456	Accept H_a
	High	$H_a: \mu_{Before} > \mu_{After}$	0.0000 (S.D. = 0.0000)	0.0001	Accept H_a
	Lumbar & Thorax BEFORE VS AFTER				
	Frequencies	Alternative Hypothesis	P-values calculated using:		Conclusion
			MatLab	JMP	
	Low	$H_a: \mu_{Before} > \mu_{After}$	0.42693 (S.D. = 0.000678315)	0.4271	Accept H_0
	High	$H_a: \mu_{Before} < \mu_{After}$	0.0000 (S.D. = 0.0000)	0.0001	Accept H_a
	Lumbar & Lumbar BEFORE VS AFTER				
	Frequencies	Alternative Hypothesis	P-values calculated using:		Conclusion
			MatLab	JMP	
	Low	$H_a: \mu_{Before} > \mu_{After}$	0.00265 (S.D. = 0.000052704)	0.0025	Accept H_a
	High	$H_a: \mu_{Before} < \mu_{After}$	0.0000 (S.D. = 0.0000)	0.0001	Accept H_a
	Lumbar & Sacrum BEFORE VS AFTER				
Frequencies	Alternative Hypothesis	P-values calculated using:		Conclusion	
		MatLab	JMP		
Low	$H_a: \mu_{Before} > \mu_{After}$	0.0000 (S.D. = 0.0000)	0.0001	Accept H_a	
High	$H_a: \mu_{Before} > \mu_{After}$	0.0033 (S.D. = 0.0000816497)	0.0034	Accept H_a	
Sacrum	Sacrum & Neck BEFORE VS AFTER				
	Frequencies	Alternative Hypothesis	P-values calculated using:		Conclusion
			MatLab	JMP	
	Low	$H_a: \mu_{Before} > \mu_{After}$	0.00331 (S.D. = 0.000073786)	0.0030	Accept H_a
	High	$H_a: \mu_{Before} < \mu_{After}$	0.002 (S.D. = 0.0000471405)	0.002	Accept H_a
	Sacrum & Thorax BEFORE VS AFTER				
	Frequencies	Alternative Hypothesis	P-values calculated using:		Conclusion
			MatLab	JMP	
	Low	$H_a: \mu_{Before} > \mu_{After}$	0.0000 (S.D. = 0.0000)	0.0001	Accept H_a
	High	$H_a: \mu_{Before} > \mu_{After}$	0.0000 (S.D. = 0.0000)	0.0001	Accept H_a
	Sacrum & Lumbar BEFORE VS AFTER				
	Frequencies	Alternative Hypothesis	P-values calculated using:		Conclusion
			MatLab	JMP	
	Low	$H_a: \mu_{Before} > \mu_{After}$	0.0000 (S.D. = 0.0000)	0.0001	Accept H_a
	High	$H_a: \mu_{Before} > \mu_{After}$	0.00329 (S.D. = 0.000031622)	0.0034	Accept H_a
	Sacrum & Sacrum BEFORE VS AFTER				
Frequencies	Alternative Hypothesis	P-values calculated using:		Conclusion	
		MatLab	JMP		
Low	$H_a: \mu_{Before} > \mu_{After}$	0.0000 (S.D. = 0.0000)	0.0001	Accept H_a	
High	$H_a: \mu_{Before} > \mu_{After}$	0.0000 (S.D. = 0.0000)	0.0001	Accept H_a	

Table 2: P-values of the bootstrap statistical test from the lower spine signals.

6. Discussion: Zero correlation nodes: Case Study I

Observe in Figure 4 the well-defined "zero correlation nodes" i.e., the common points of intersection of all the $r_{ij}(s)$ versus s curves and the $r = 0$ axis, strong evidence of a coherent standing wave. Both the s_1 nodes and to a less extent the s_2 nodes are visible (marked with solid and dotted circles, resp.). Also

note the consistency between the synchronization doublet of Figure 3, sacrum, and the s_1 node of Figure 4, sacrum (d), both of them identified with a diamond \diamond . As such, it is fair to say that the results of [2] have been reproduced in an environment deliberately taken not as “clean” as that of [2].

However, the same results are not as visually obvious for Case Study II when a “bifurcation” occurs.

7. Discussion: Case Study II

Before the bifurcation, the “zero correlation nodes” are somehow clear on the D_8 subband as shown in Figure 13, but markedly depleted on the D_7 and D_6 subbands, as shown in Figures 14 and 15, respectively.

Observe the consistency between the synchronization doublets of Figure 10 and the s_1 node of Figure 13, neck (a), marked with a box \square . We have the same consistency between the synchronization doublets of Figure 11 and the s_1 node of Figure 14, thorax (b), marked with a triangle \triangle .

After the bifurcation, the D_8 subband is no longer the best to reveal coherence as shown in Figures 16a-16d. Contrarily to [2] and Case-Study I of the present paper, the D_7 subband of the signals restricted from sample 5,411 to 9,871 exhibits better zero correlation nodes as shown in Figures 17a-17d.

The qualitative behavior of Figure 19 happens to be correct for the lower spinal signals, as demonstrated by the statistical test of significance, where a depletion of the low frequency component occurs predominantly *after the bifurcation*. Furthermore, this statistical test corroborates the zero correlation nodes pattern that takes place on two different subbands when the system passes through a bifurcation.

It is thus fair to say that, before the bifurcation, the coherence is at the D_8 level, while, after the bifurcation, the coherence is at the D_7 level.

Comparing the D_8 and the D_7 correlation plots, it is clear that the latter reveal a coherent movement twice as fast as the former. Therefore, the passage from a coherence standing wave on D_8 to a coherent standing wave on D_7

means that the standing wave doubles its speed across the bifurcation. This phenomenon is somehow the reverse of the well-known period doubling phenomenon in chaos [9].

8. Conclusion

First, in Case Study I, we illustrated the reproducibility of the results of [2] indicating that the spinal wave is a coherent movement elicited by a Central Pattern Generator. Here *reproducibility* spans across a period of 10 years, during which many changes in the protocol and the experimental hardware occurred, hence demonstrating the "robustness" of the results. Ref. [2] as well as Case-Study I have demonstrated coherence at the D_8 subband of the DB3 wavelet decomposition. Second, the really novel result here is the observation that the standing wave can undergo bifurcation with a shift of the coherence from D_8 to D_7 . More practically speaking, this means that the motion speeds by a factor of 2, in a process that appears to be the reverse of the well-known period doubling [10] in dynamical systems theory.

The statistical test of difference between the means on the cross Power Spectral Density corroborates the shift of zero correlation nodes from D_8 subband, before the bifurcation, to D_7 subband, after the bifurcation. This statistical test also confirms a continuous change in the power spectrum of the signal as the system passes through a period doubling bifurcation, at low frequencies the power of the signal before the bifurcation turned out to be statistically significantly higher than the signal after the bifurcation with a 95% confidence level, the previous happens to be prevalent among the lower spine signals (lumbar spine and sacrum).

All of the above applies to the so-called Level 2 wave, characterized by one single mode shape node. A more complicated wave with two mode shape nodes can be elicited, but with more difficulties though. Whether this more complicated wave could undergo bifurcation is entirely open and is left for further studies.

References

- [1] N. Kopell, We got rhythm: Dynamical systems of the nervous system, Notices of the American Mathematical Society 47 (1).
- [2] E. Jonckheere, P. Lohsoonthorn, S. Musuvathy, V. Mahajan, M. Stefanovic, On a standing wave central pattern generator and the coherence problem, Biomedical Signal Processing and Control (2010) 336–347.
- [3] A. Breig, Adverse Mechanical Tension in the Central Nervuous System, John Wiley, New York, 1987.
- [4] A. Tilton, P. G. Mehta, Control with rhythms: A CPG architecture for pumping a swing, in: American Control Conference (ACC), Portland, Oregon, USA, 2014.
- [5] Y. A. Kuznetsov, Elements of Applied Bifurcation Theory. Applied Mathematical Sciences, Vol. 112, Springer-Verlag New York, Inc., 1998.
- [6] S. Day, Important factors in surface emg measurement, Tech. rep., Bortec Biomedical Ltd, 225, 604-1st St. Sw, Calgary, AB, T2P 1M7, Canada (2000).
- [7] M. G. Bulmer, Principles of Statistics, Dover, 1979.
- [8] W. Mendenhall, T. Sincich, Statistics for Engineering and the Sciences, 5th Edition, Prentice Hall, 2007.
- [9] T. Tel, M. Gruiz, Chaotic Dynamics: An Introduction Based on Classical Mechanics, Cambridge University Press, Budapest, 2006.
- [10] D. W. Berns, J. L. Moiola, G. Chen, Predicting period-doubling bifurcations and multiple oscillations in nonlinear time-delayed feedback systems, IEEE Transactions on Circuits and Systems I: Fundamental Theory and Applications 45 (7).

Appendix A. Statistical Test. Convergence of p-values.

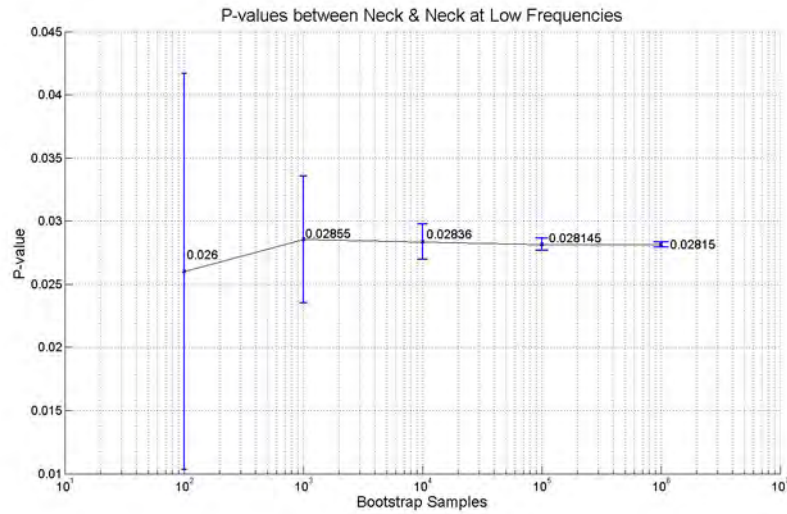


Figure Appendix A.1: Convergence at 0.02815 of the p-value between Neck and Neck at low frequencies.

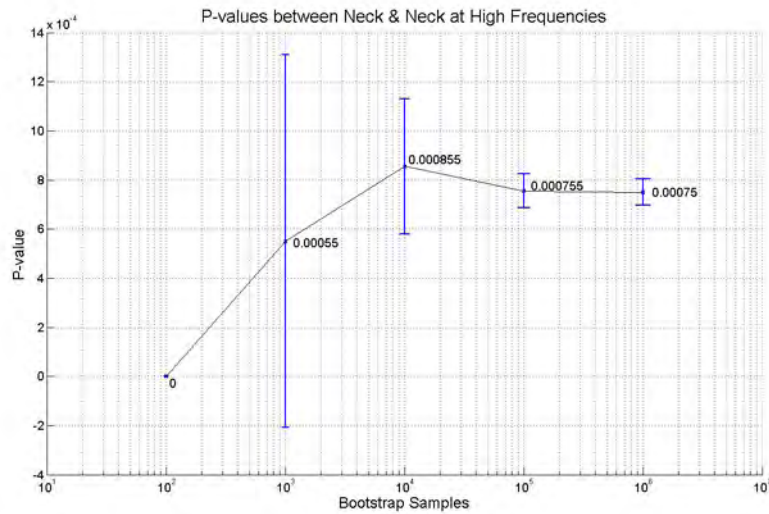


Figure Appendix A.2: Convergence at 0.00075 of the p-value between Neck and Neck at high frequencies.

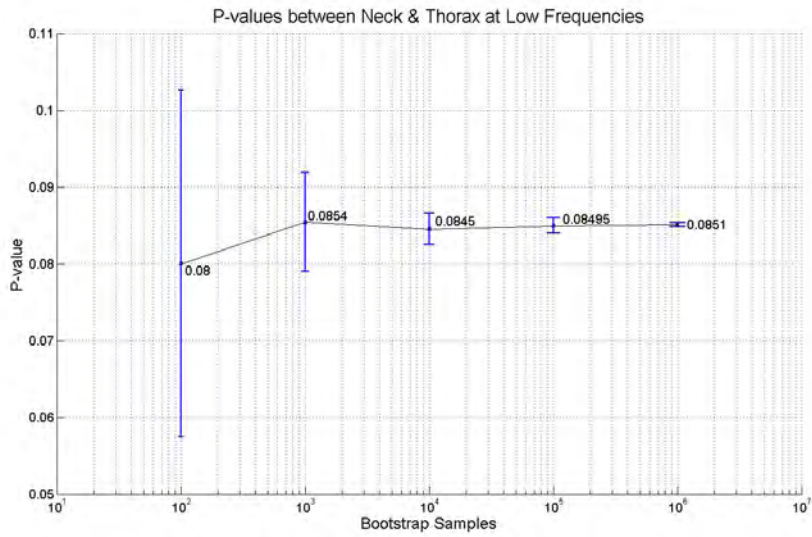


Figure Appendix A.3: Convergence at 0.0851 of the p-value between Neck and Thorax at low frequencies.

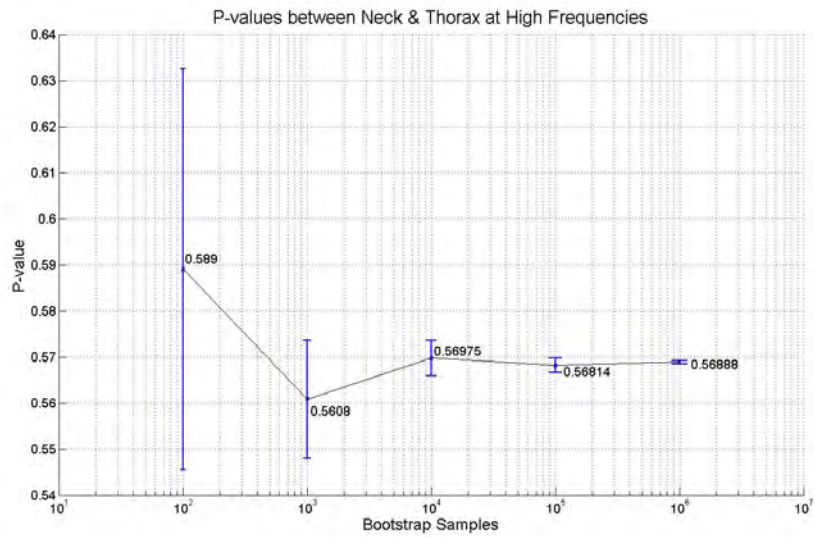


Figure Appendix A.4: Convergence at 0.56888 of the p-value between Neck and Thorax at high frequencies.

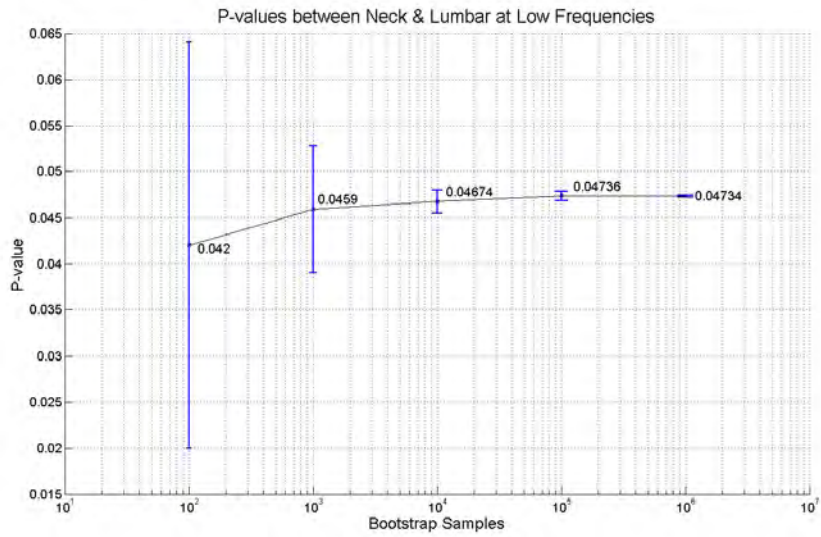


Figure Appendix A.5: Convergence at 0.04734 of the p-value between Neck and Lumbar at low frequencies.

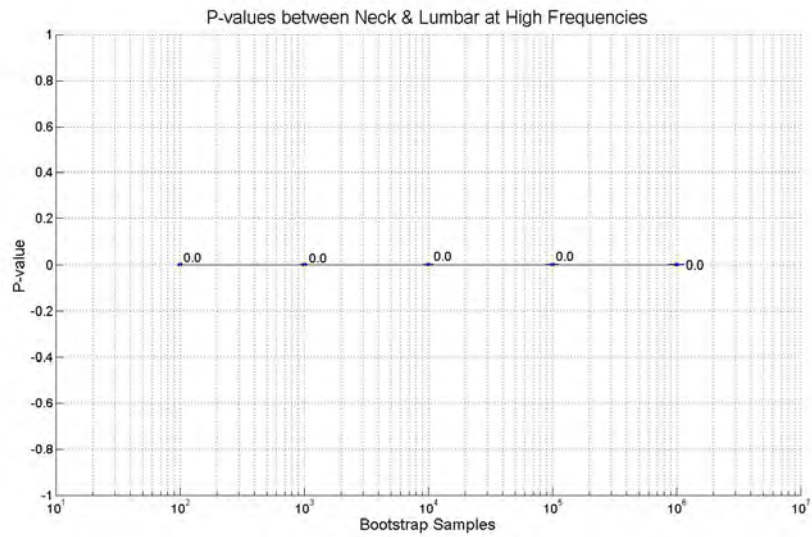


Figure Appendix A.6: Convergence at 0.0 of the p-value between Neck and Lumbar at high frequencies.

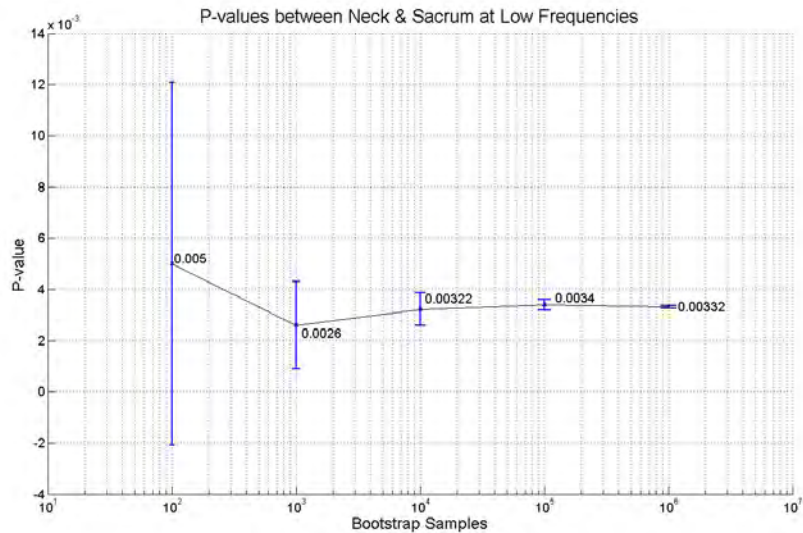


Figure Appendix A.7: Convergence at 0.00332 of the p-value between Neck and Sacrum at low frequencies.

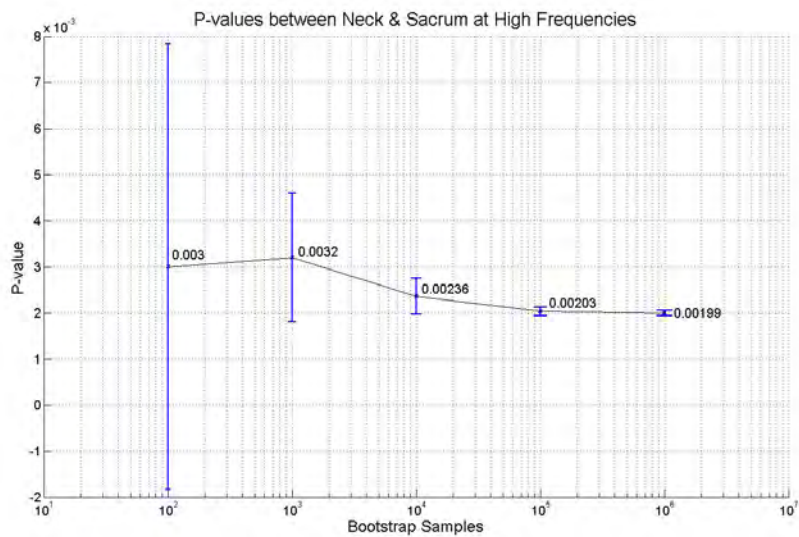


Figure Appendix A.8: Convergence at 0.00199 of the p-value between Neck and Sacrum at high frequencies.

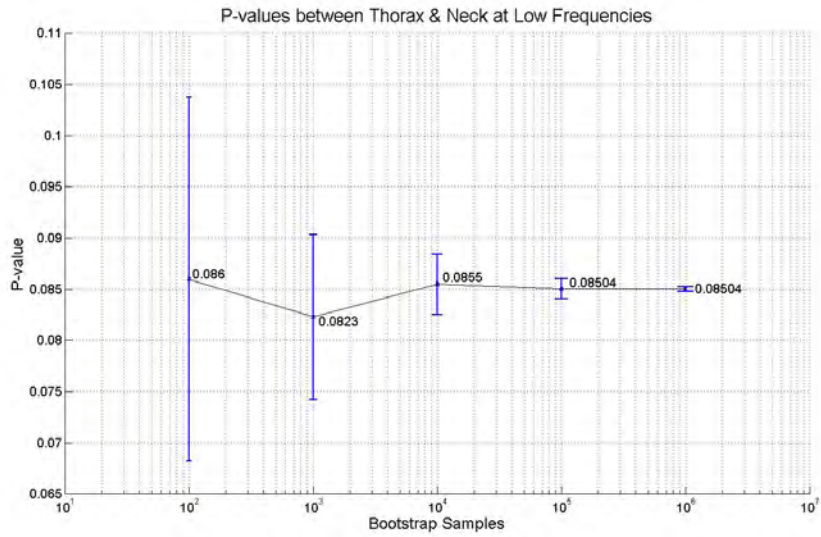


Figure Appendix A.9: Convergence at 0.08504 of the p-value between Thorax and Neck at low frequencies.

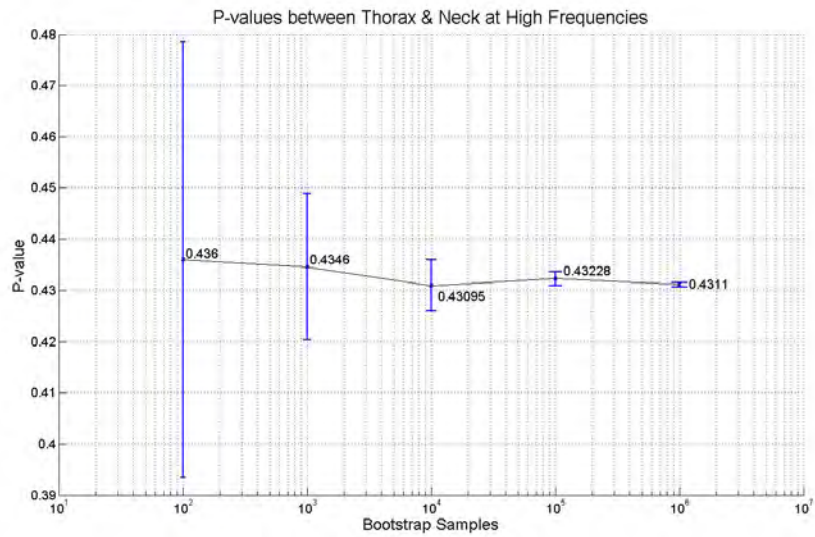


Figure Appendix A.10: Convergence at 0.4311 of the p-value between Thorax and Neck at high frequencies.

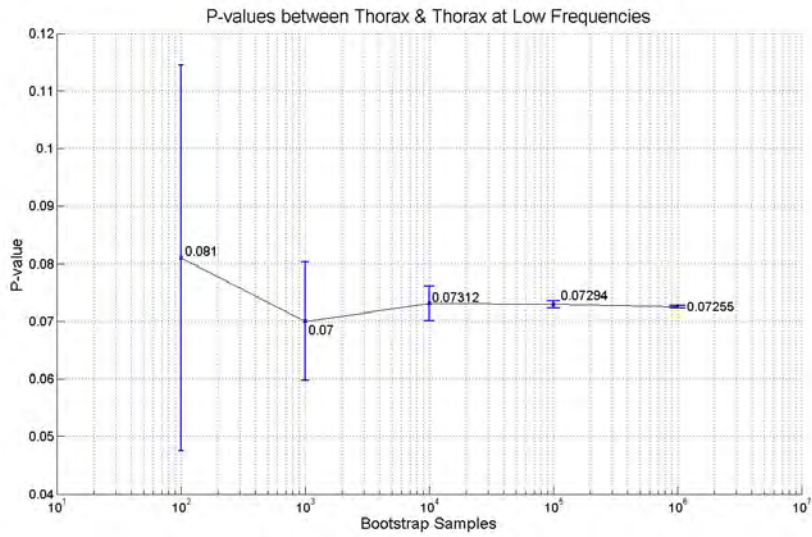


Figure Appendix A.11: Convergence at 0.07255 of the p-value between Thorax and Thorax at low frequencies.

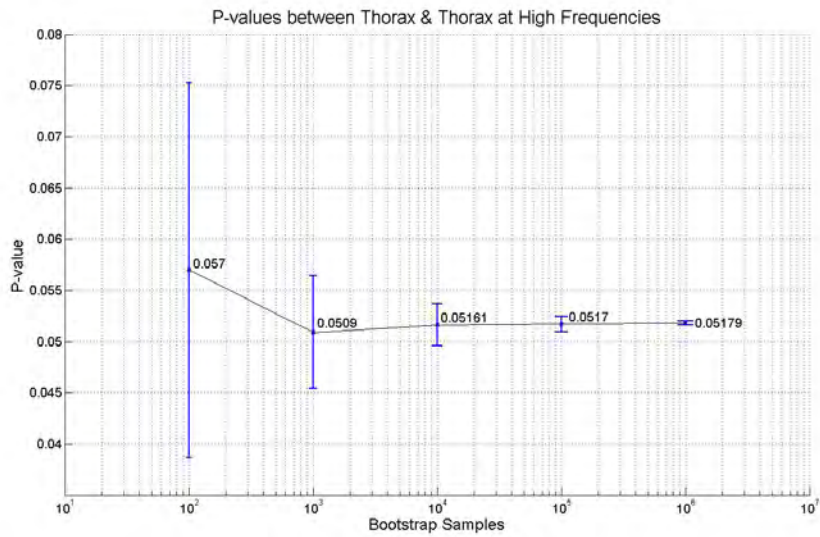


Figure Appendix A.12: Convergence at 0.05179 of the p-value between Thorax and Thorax at high frequencies.

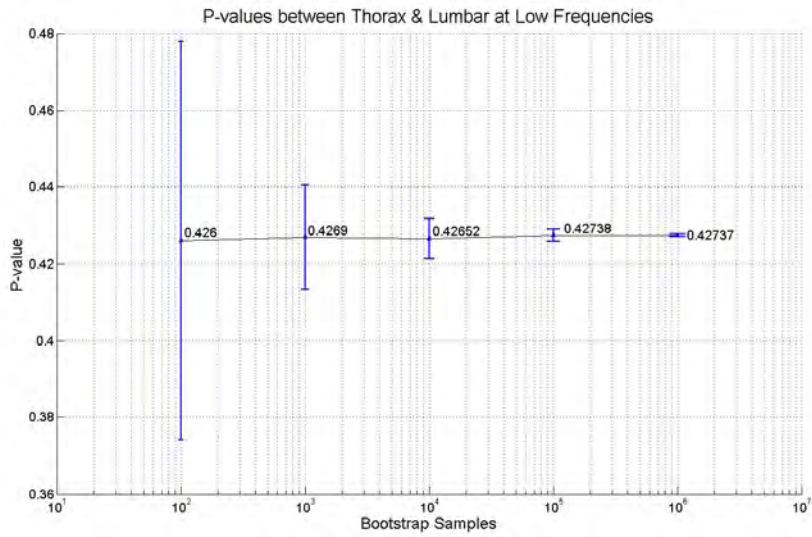


Figure Appendix A.13: Convergence at 0.42737 of the p-value between Thorax and Lumbar at low frequencies.

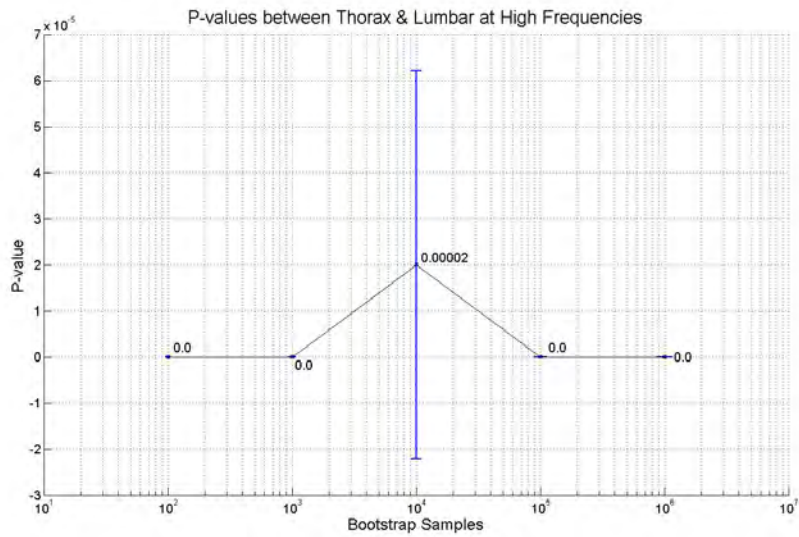


Figure Appendix A.14: Convergence at 0.0 of the p-value between Thorax and Lumbar at high frequencies.

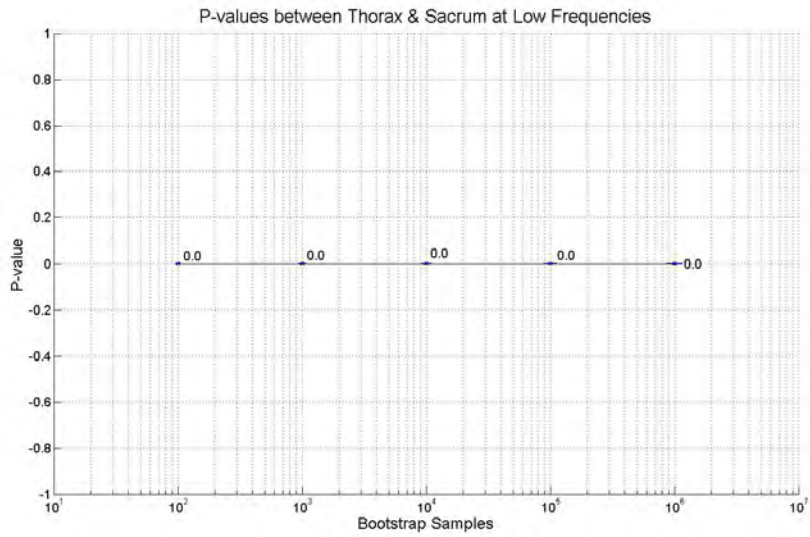


Figure Appendix A.15: Convergence at 0.0 of the p-value between Thorax and Sacrum at low frequencies.

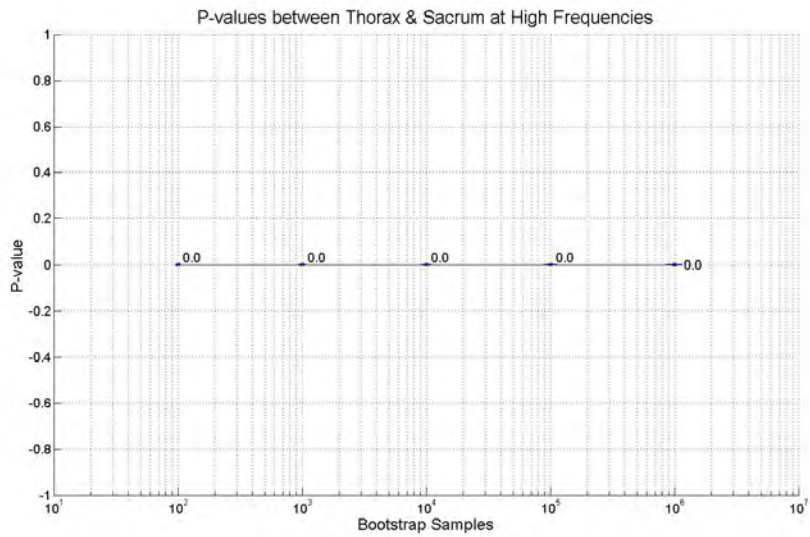


Figure Appendix A.16: Convergence at 0.0 of the p-value between Thorax and Sacrum at high frequencies.

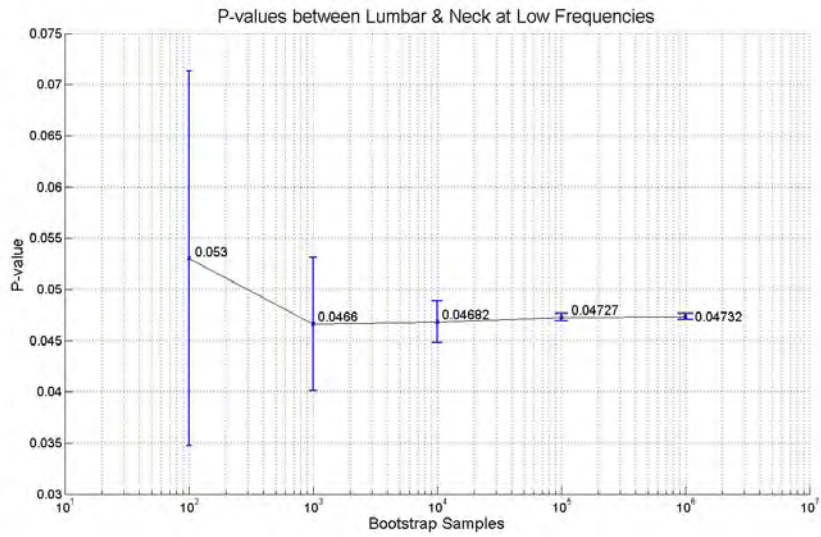


Figure Appendix A.17: Convergence at 0.0732 of the p-value between Lumbar and Neck at low frequencies.

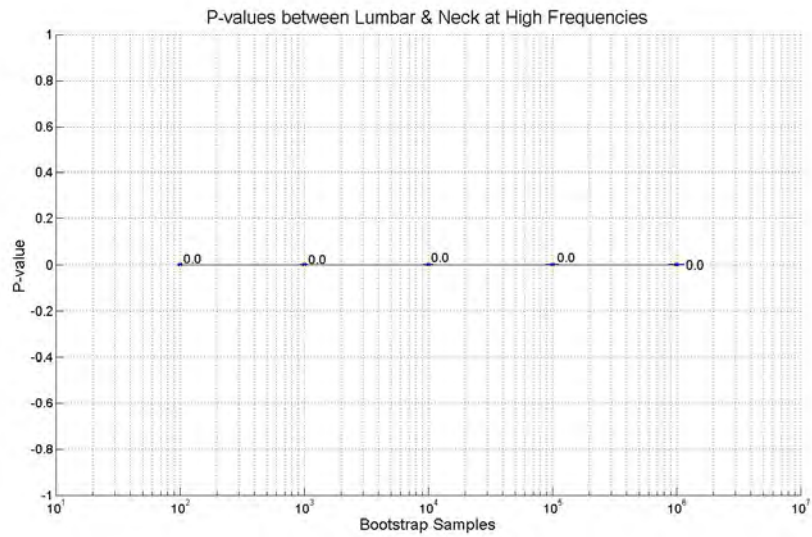


Figure Appendix A.18: Convergence at 0.0 of the p-value between Lumbar and Neck at high frequencies.

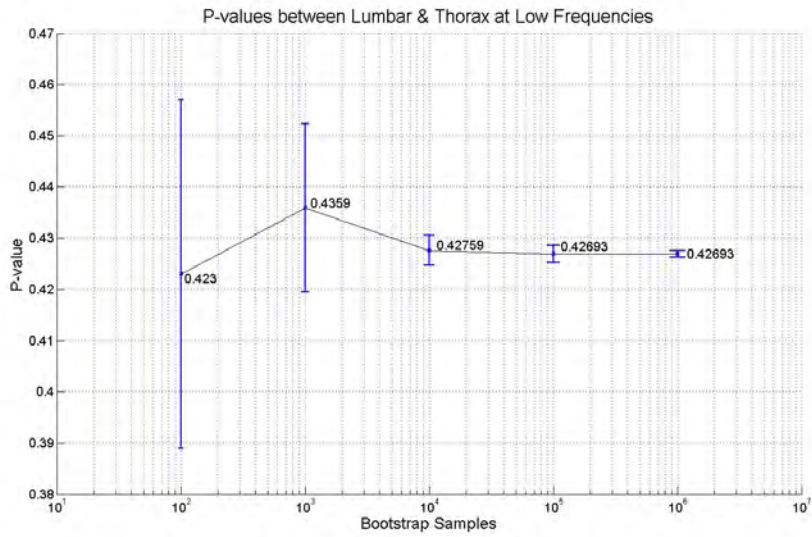


Figure Appendix A.19: Convergence at 0.42693 of the p-value between Lumbar and Thorax at low frequencies.

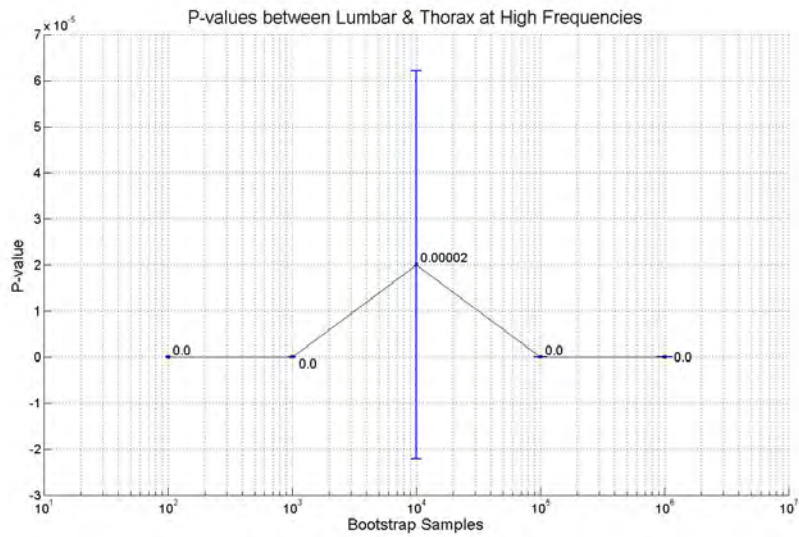


Figure Appendix A.20: Convergence at 0.0 of the p-value between Lumbar and Thorax at high frequencies.

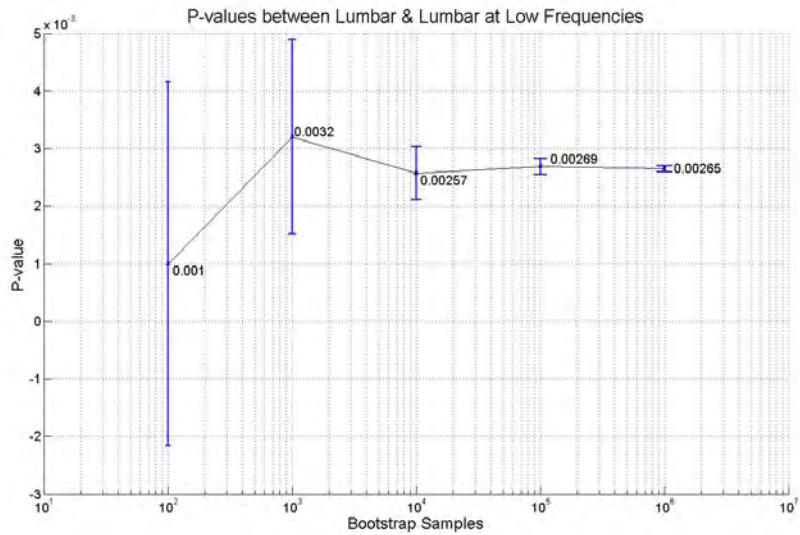


Figure Appendix A.21: Convergence at 0.00265 of the p-value between Lumbar and Lumbar at low frequencies.

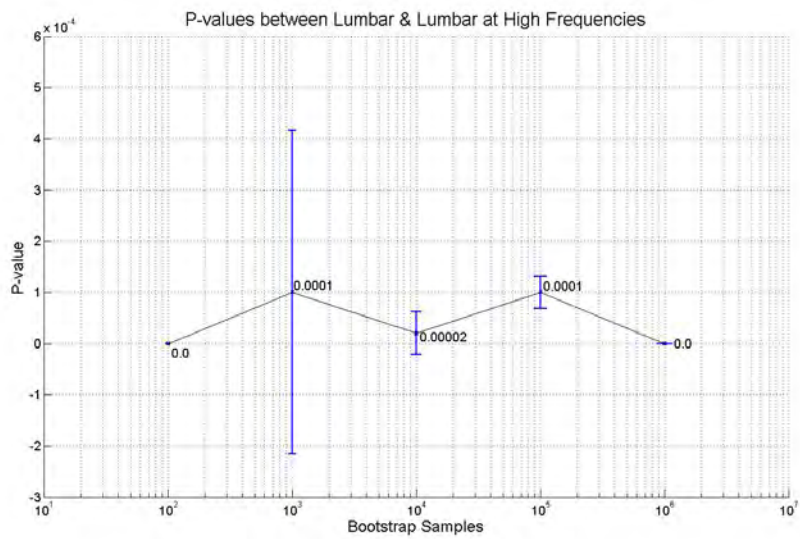


Figure Appendix A.22: Convergence at 0.0 of the p-value between Lumbar and Lumbar at high frequencies.

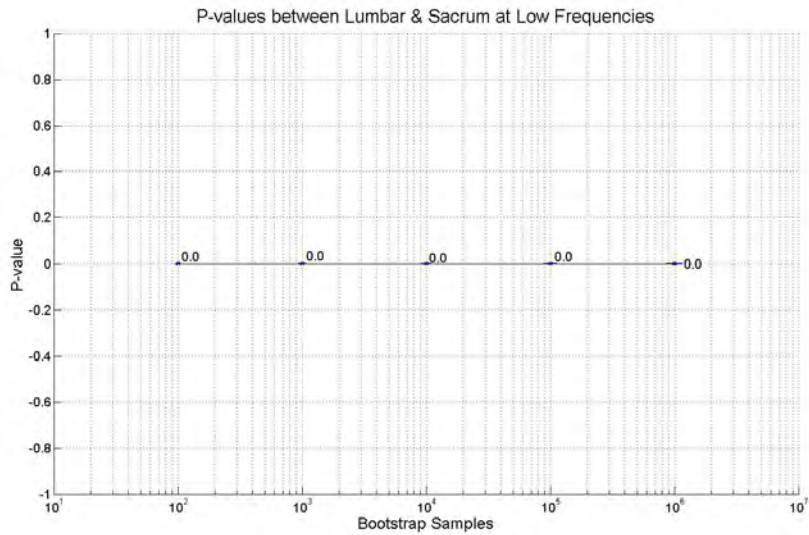


Figure Appendix A.23: Convergence at 0.0 of the p-value between Lumbar and Sacrum at low frequencies.

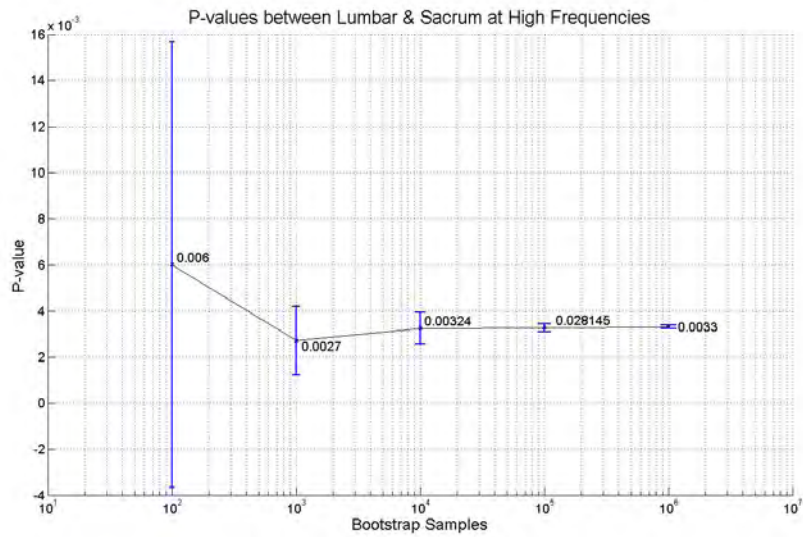


Figure Appendix A.24: Convergence at 0.0033 of the p-value between Lumbar and Sacrum at high frequencies.

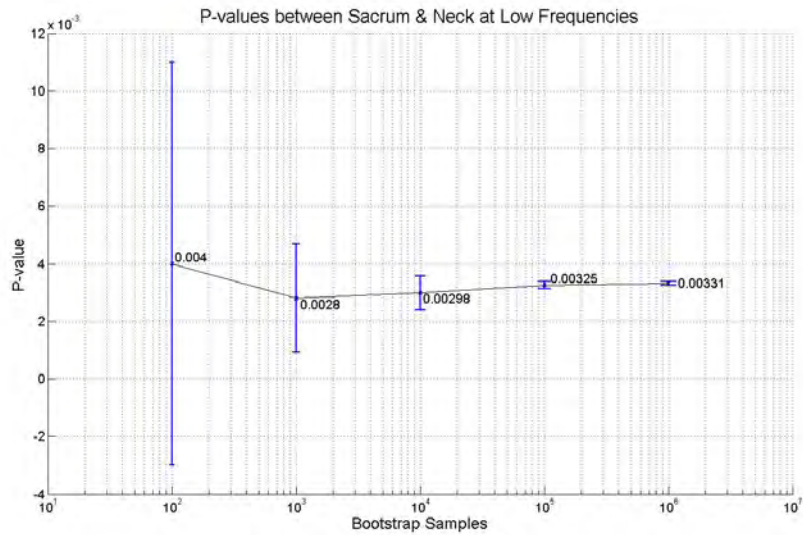


Figure Appendix A.25: Convergence at 0.00331 of the p-value between Sacrum and Neck at low frequencies.

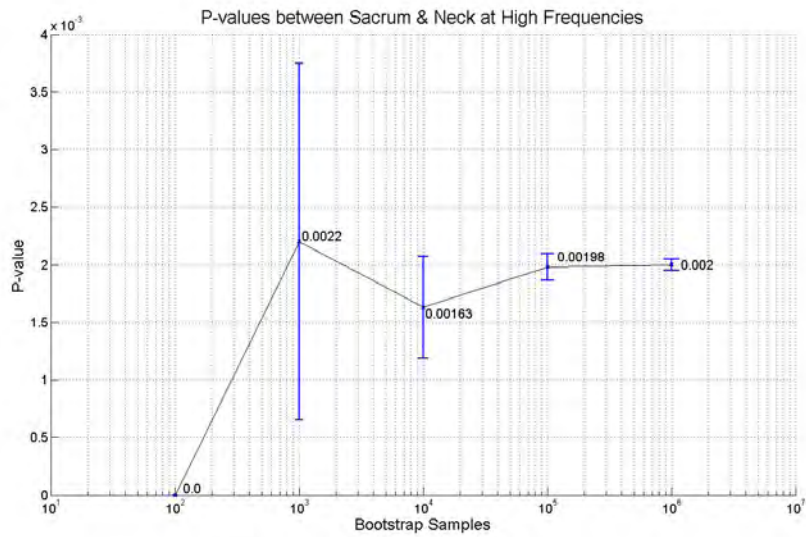


Figure Appendix A.26: Convergence at 0.002 of the p-value between Sacrum and Neck at high frequencies.

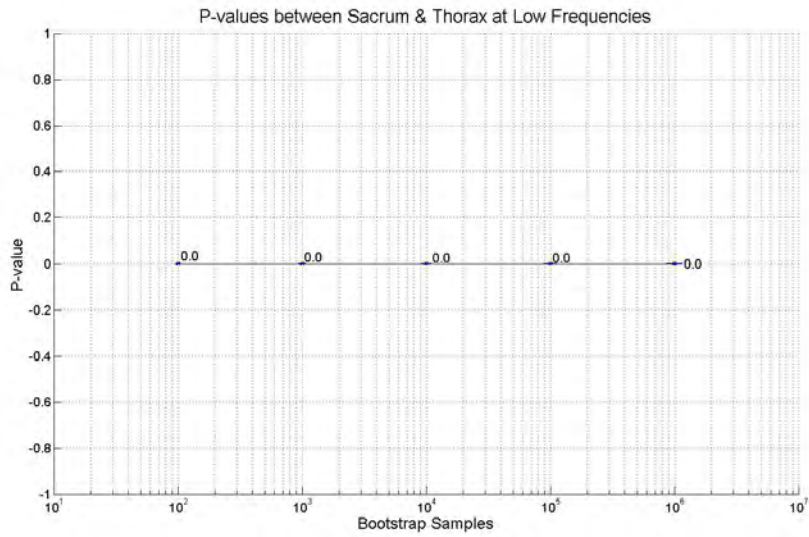


Figure Appendix A.27: Convergence at 0.0 of the p-value between Sacrum and Thorax at low frequencies.

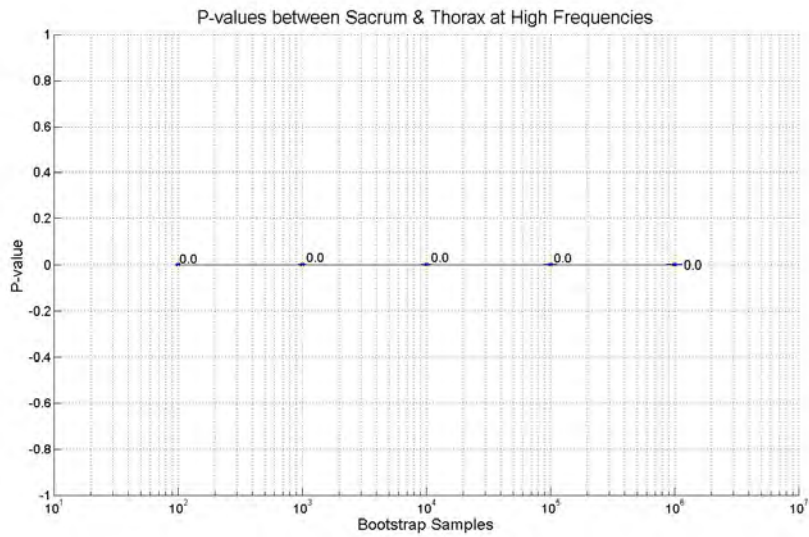


Figure Appendix A.28: Convergence at 0.0 of the p-value between Sacrum and Thorax at high frequencies.

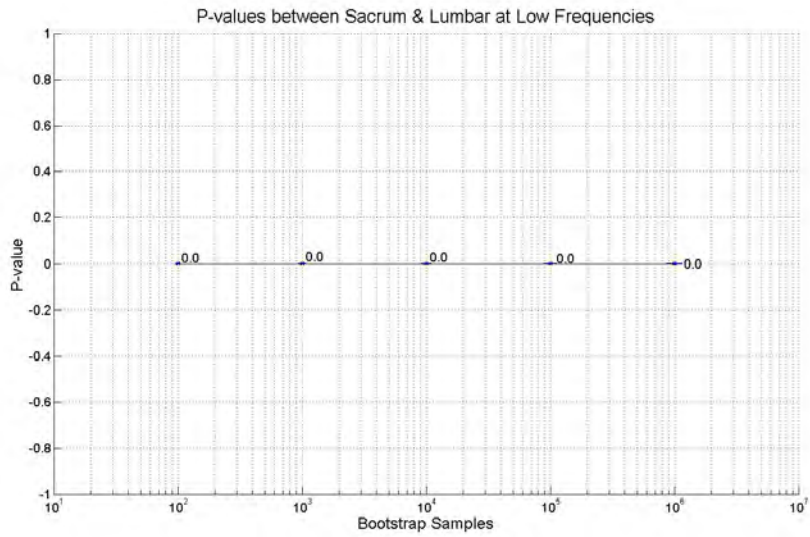


Figure Appendix A.29: Convergence at 0.0 of the p-value between Sacrum and Lumbar at low frequencies.

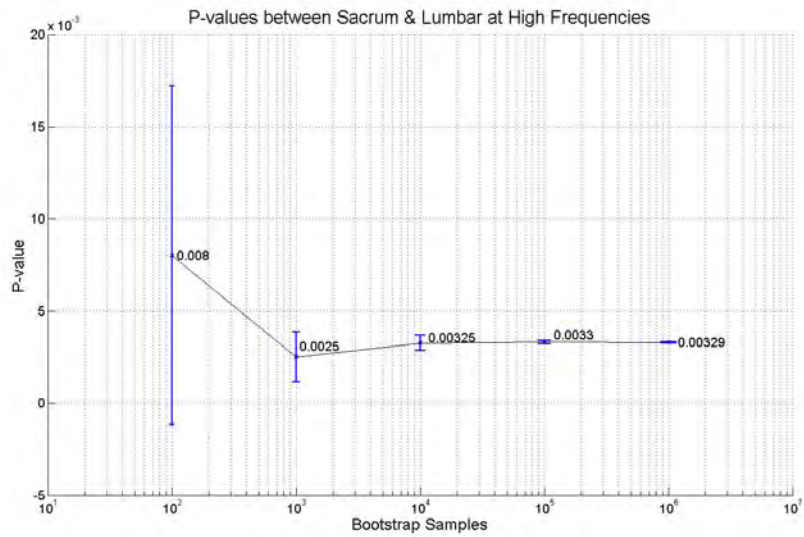


Figure Appendix A.30: Convergence at 0.00329 of the p-value between Sacrum and Lumbar at high frequencies.

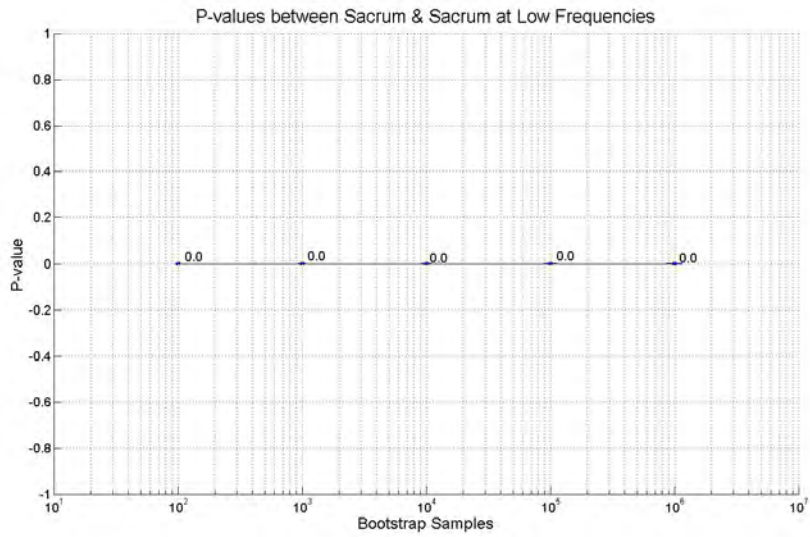


Figure Appendix A.31: Convergence at 0.0 of the p-value between Sacrum and Sacrum at low frequencies.

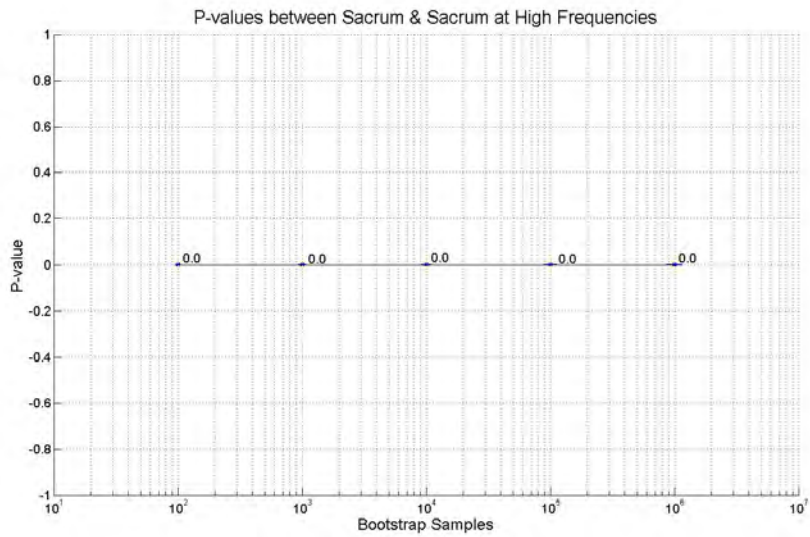


Figure Appendix A.32: Convergence at 0.0 of the p-value between Sacrum and Sacrum at high frequencies.